Acta Crystallographica Section B
Structural Science
ISSN 0108-7681

Single-crystal structure refinement of $NaTiSi_2O_6$ clinopyroxene at low temperatures ($298 < T < 100$ K)

Günther J. Redhammer,[a,b]*‡ Haruo Ohashi[c] and Georg Roth[a]

[a]Institute of Crystallography, Rheinisch-Westfälische Technical Highschool Aachen, Jägerstrasse 17/19, D-52056 Aachen, Germany, [b]Institute of Mineralogy, University Salzburg, Hellbrunnerstrasse 34, A-5020 Salzburg, Austria, and [c]HASHI Institute for Silicate Science, Nishinakanobu 1-9-25, Shinagawa, Tokyo 142-0054, Japan

‡ Corresponding address: A-4910 Neuhofen i.I. 224/1, Austria.

Correspondence e-mail: guenther.redhammer@aon.at

Received 17 June 2003
Accepted 2 October 2003

The alkali-metal clinopyroxene $NaTi^{3+}Si_2O_6$, one of the rare compounds with trivalent titanium, was synthesized at high temperature/high pressure and subsequently investigated by single-crystal X-ray diffraction methods between 298 and 100 K. One main difference between the high- and the low-temperature form is the sudden appearance of two different $Ti^{3+}-Ti^{3+}$ interatomic distances within the infinite chain of the TiO_6 octahedra just below 197 K. This change can be seen as direct evidence for the formation of Ti—Ti singlet pairs in the low-temperature phase. Mean Ti—O bond lengths smoothly decrease with decreasing temperature and the phase transition is associated with a slight jump in the Ti—O bond length. The break in symmetry, however, causes distinct variations, especially with respect to the two $Ti-O_{apex}$ bond lengths, but also with respect to the four Ti—O bonds in the equatorial plane of the octahedron. The TiO_6 octahedron appears to be stretched in the chain direction with a slightly larger elongation in the $P\bar{1}$ low-temperature phase compared with the $C2/c$ high-temperature phase. Polyhedral distortion parameters such as bond-length distortion and octahedral angle variance suggest the TiO_6 octahedron in $P\bar{1}$ to be closer to the geometry of an ideal octahedron than in $C2/c$. Mean Na—O bond lengths decrease with decreasing temperature and the variations in individual Na—O bond lengths are the result of variations in the geometry of the octahedral site. The tetrahedral site acts as a rigid unit, which does not show pronounced changes upon cooling and through the phase transitions. There are neither large changes in bond lengths and angles nor in polyhedral distortion parameters, for the tetrahedral site, when they are plotted. In contrast with the $C2/c \rightarrow P2_1/c$ phase transition, found especially in $LiMSi_2O_6$ clinopyroxenes, no very large variations are found for the tetrahedral bridging angle. Thus, it is concluded that the main factor inducing the phase transition and controlling the structural variations is the $M1$ octahedral site.

1. Introduction

Very recently, the list of compounds with spin-1/2 linear chains and spin-Peierls-like transitions has been extended to include $NaTiSi_2O_6$ and $LiTiSi_2O_6$ (Isobe *et al.*, 2002; Konstantinović *et al.*, 2003). Both compounds belong to the alkali-metal pyroxene family (general formula $A^+M^{3+}Si_2O_6$), which have been widely investigated from mineralogical and crystallographic standpoints in the past (*e.g.* Ohashi, 2003; Redhammer & Roth, 2003*a*,*b*; Redhammer *et al.*, 2001; Ohashi, 1981; Hawthorne & Grundy, 1974, Clark *et al.*, 1969). Recently, such clinopyroxenes with transition elements M^{3+}

have drawn attention as low-dimensional magnets. Their structure contains one-dimensional $M^{3+}O_6$ octahedral chains along the crystallographic *c* direction, which are bridged by SiO_4 tetrahedra. The magnetic interaction between these neighbouring $M^{3+}O_6$ chains *via* the tetrahedral chains is much smaller than the interaction within the octahedral chains.

The synthesis of $NaTiSi_2O_6$ single crystals and the full description of the room-temperature structure was first performed by Ohashi (2003) and Ohashi *et al.* (1982). At 298 K, the compound has monoclinic symmetry with the space group *C*2/*c*. Recently, Isobe *et al.* (2002) synthesized $NaTiSi_2O_6$ as a powder sample under ambient pressure and reported the structural, thermal and magnetic properties of $NaTiSi_2O_6$. They found Curie–Weiss behaviour with regard to the temperature dependence of the magnetic susceptibility in the high-temperature region and a sharp decrease of the magnetic susceptibility (gap-like behaviour) below 210 K. From specific heat measurements, the entropy change was estimated to be $\Delta S = 2.8$ J mol^{-1} K^{-1}, which is approximately half the theoretical value expected for a purely magnetic phase transition (Isobe *et al.*, 2002). Thus, an additional structural phase transition was expected and found. Some X-ray diffraction peaks in their powder diffraction experiments split into two peaks below 210 K, suggesting a triclinic low-temperature phase of $NaTiSi_2O_6$. An X-ray diffraction pattern taken at 10 K was indexed in a triclinic metric with lattice parameters $a = 6.63$, $b = 8.83$, $c = 5.39$ Å, $\alpha = 90.2$, $\beta = 102.3$, $\gamma = 47.1^\circ$. In a conference proceedings paper, Ninomiya *et al.* (2003) describe a similar unit cell for the low-temperature phase, with the space group $P\bar{1}$. For their low-temperature structural model, two crystallographic independent positions for Ti^{3+} and thus two different Ti—Ti interatomic distances were found. This was seen as direct evidence for the formation of Ti^{3+}–Ti^{3+} singlet pairs. Their structural model was based on a 1.8196 Å wavelength neutron diffraction experiment on a powder sample at 10 K. No atomic coordinates or additional structural parameters are available for the low-temperature structure of $NaTiSi_2O_6$.

Motivated by the availability of high-quality single crystals from high-pressure synthesis experiments, the aim of our present study is to:

(i) verify the presence of a temperature-induced phase transition in $NaTiSi_2O_6$,

(ii) determine the unknown low-temperature structure,

(iii) verify the given triclinic unit cell and

(iv) study the changes in the crystal structure between 298 and 100 K.

Some aspects of the crystal chemistry of sodium clinopyroxenes are also discussed.

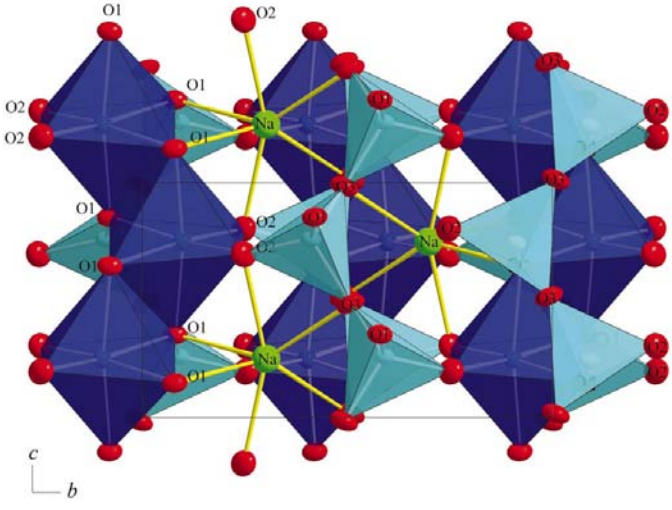

Figure 1
Structure of $NaTiSi_2O_6$ at 200 K viewed along [100].

2. Experimental

2.1. Synthesis of crystals

The single crystals were produced by a solid-state reaction using a belt-type high-pressure apparatus (Fukunaga *et al.*, 1979). The starting material was a stoichiometric mixture of $Na_2Si_2O_5$, Ti_2O_3 and SiO_2. The mixture was contained in a carbon capsule and heated at 1773 K under a pressure of 5 GPa for 12 h. This procedure led to prismatic needle-like crystals up to 0.15 mm in length. The crystals used in this study are the same as those used by Ohashi *et al.* (1982), except that the sample used in this study had been stored at 1 atm and room temperature for 21 years.

2.2. Single-crystal X-ray diffraction

A dark blue, prismatic crystal of $NaTiSi_2O_6$ was used for single-crystal X-ray diffraction experiments. Intensity data sets were collected on a Stoe IPDS II image-plate diffractometer system, equipped with a cryostream liquid N_2 cryostat (85–300 K, accuracy at least 1 K). Intensity data were collected within an ω range of 0–180° and two different φ positions in most cases; the ω rotation during exposure was 1.5° per frame. This procedure yields a completeness of data sets that exceeds 95%. Data sets were collected at 100, 110, 130, 140, 150, 160, 170, 180 190, 200, 210, 215, 220, 240, 260 and 298 K. All lattice parameters were determined from single-crystal X-ray diffraction data. An absorption correction was performed empirically *via* symmetry equivalents using the *SHAPE* program (Stoe & Cie, 1996). The maximum transmission calculated in this way was $T_{max} = 0.72$–0.74 for all data sets and the minimum transmission $T_{min} = 0.62$–0.64. Structure solution (using Patterson methods) and subsequent refinement was carried out with the programs *SHELXS*97 (Sheldrick 1997*a*) and *SHELXL*97 (Sheldrick, 1997*b*), as implemented in the program suite *WinGX*1.64 (Farrugia, 1999). X-ray scattering factors in their ionic form, together with anomalous dispersion coefficients, were taken from the *International Tables for Crystallography* (Wilson, 1992).

In most of the figures the regression lines were fitted to the data to clarify trends. These regressions correspond to polynomials of first (linear) or second (quadratic) order: $y = a_o + a_1^* x + a_2^* x^2$. Second-order polynomial functions were used

when distinct curvatures were visible to the eye in the data curves. Regression R^2 values were above 0.9 in almost all fits.

3. Results and discussion

3.1. Structure of $NaTiSi_2O_6$ at 298 K compared with $NaM^{3+}Si_2O_6$

The structure of $NaTiSi_2O_6$ is consistent with that found by Ohashi *et al.* (1982) and Ohashi (2003) and fits well into the structural topology, valid for other $NaM^{3+}Si_2O_6$ clinopyroxenes. The lattice parameters for $NaTiSi_2O_6$ determined here differ slightly from those of Ohashi *et al.* (1982) and Ohashi (2003), most probably owing to the different quenchability from high-pressure conditions. The structure of $NaTiSi_2O_6$ is isomorphous with the other $NaM^{3+}Si_2O_6$ clinopyroxenes, where M^{3+} = Al, Cr, Ga, Fe, V, Mn, Sc and In. Table 1 summarizes the basic structural parameters and literature references for $NaM^{3+}Si_2O_6$ compounds, for which a reference is given in the Inorganic Crystal Structure Database (ICSD). The metal cations occupy the *M*1 octahedra, which are edge-sharing to form an infinite zigzag chain parallel to the crystallographic *c* axis (Fig. 1). Sodium occupies the sixfold *M*2 site. As experience shows, the *M*1 chain is a more rigid unit than the corner-sharing tetrahedra of the silicate chain. Thus, the various distortions of the clinopyroxene structure partly arise from the different space requirements of these structural units (*e.g.* Cameron *et al.*, 1973; Hawthorne & Grundy, 1977; Redhammer & Roth, 2003*a*).

As the data in Table 1 show, the structural variations across the $NaM^{3+}Si_2O_6$ series are largely controlled by the size of the *M*1 cation. Fig. 2(*a*) displays the variation of the average *M*1—O bond lengths *versus* the ionic radius of the *M*1 cation. A positive linear correlation is found; however, data for the $Na(Sc,In)Si_2O_6$ solid solution series deviate slightly from this, as do the data of $NaGaSi_2O_6$. The average *M*1—O bond length for $NaTiSi_2O_6$ [2.054 (2) Å] excellently fits the trend observed in the literature data. The deviation of individual bond lengths from their mean value (bond-length distortion, BLD; Renner

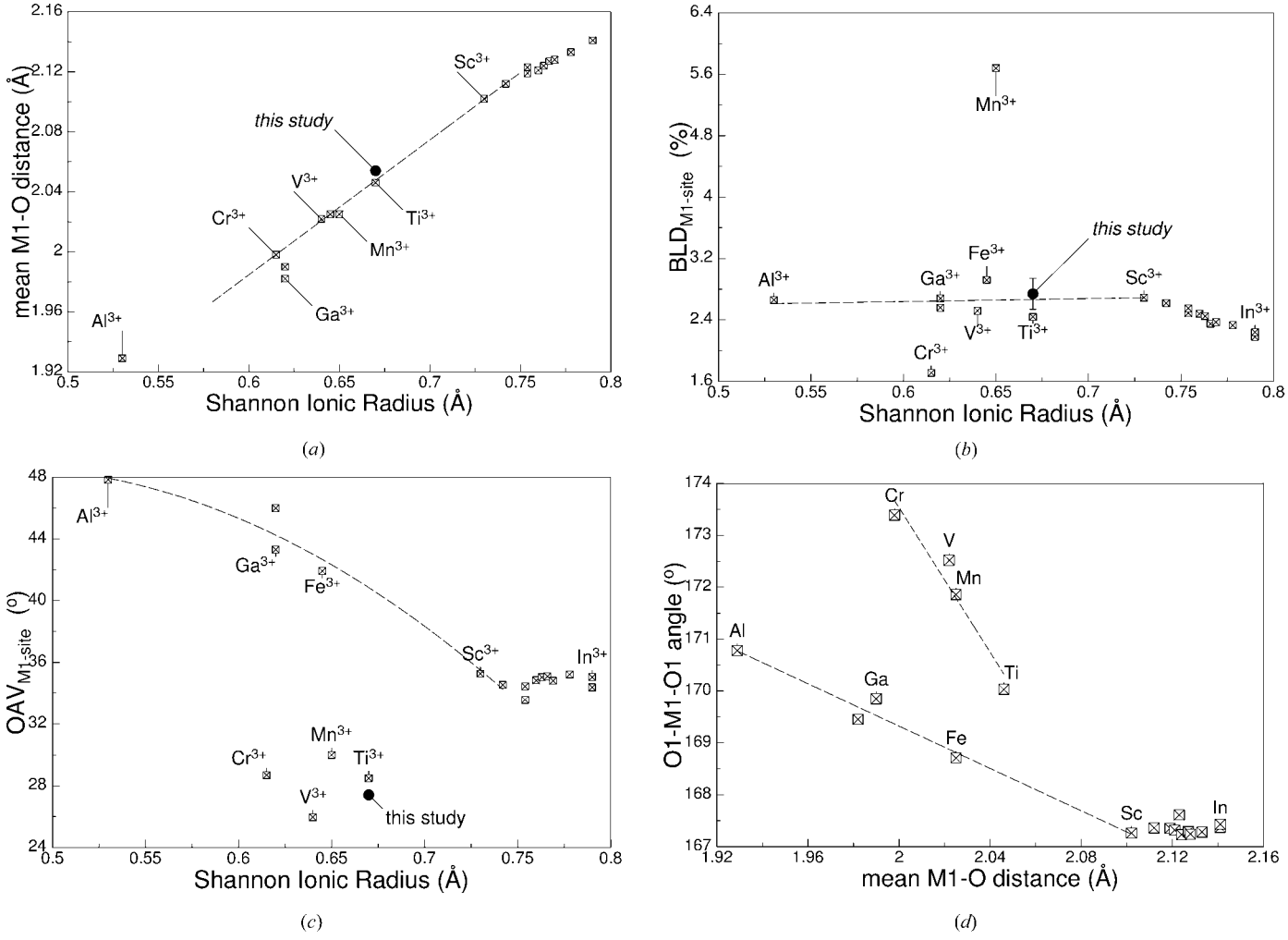

Figure 2
Structural parameters of the *M*1 site plotted *versus* the ionic radius of the *M*1 site (r_{M1}) cation for various $NaM^{3+}Si_2O_6$ clinopyroxenes. The structural reference for individual compounds is given in Table 1. (*a*) Average *M*1—O bond lengths *versus* r_{M1}; (*b*) bond-length distortion parameter BLD (Renner & Lehmann, 1986) *versus* r_{M1}; (*c*) quadratic octahedral angle variance (OAV; Toraya, 1981) *versus* r_{M1}; (*d*) octahedral O1—*M*1--O1 bond angle *versus* average *M*1—O bond length. Error bars for the literature data are not shown but are larger than that for $NaTiSi_2O_6$, investigated in this study.

Table 1
Selected structural (from the ICSD) and some polyhedral distortion parameters of $NaM^{3+}Si_2O_6$ clinopyroxenes.

Compound	ICSD No.	Ref.	Radius (Å)	a (Å)	b (Å)	c (Å)	β (°)	Volume (Å)	$\langle M1-O\rangle$ (Å)	BLD_{oct} (%)	OAV (°)	$\langle M2-O\rangle_6$ (Å)	$\langle T-O\rangle$ (Å)	BLD_{tet} (%)	TAV (°)
$NaAlSi_2O_6$	15489	(*a*)	0.53	9.418	8.562	5.219	107.58	401.19	1.929	2.7	47.8	2.378	1.625	1.4	24.5
$NaCrSi_2O_6$	9670	(*b*)	0.615	9.550	8.712	5.272	107.44	418.47	1.998	1.7	28.7	2.396	1.624	1.7	15.7
$NaGaSi_2O_6$	80828	(*c*)	0.62	9.5573	8.7019	5.2705	107.637	417.73	1.990	2.6	43.31	2.398	1.627	1.6	15.5
$NaGaSi_2O_6$	39195	(*d*)	0.62	9.557	8.679	5.260	107.68	415.68	1.982	2.7	46.0	2.399	1.625	1.4	14.9
$NaVSi_2O_6$	78342	(*e*)	0.64	9.6339	8.7413	5.296	106.905	426.72	2.022	2.5	26.0	2.401	1.628	1.5	15.6
$NaFeSi_2O_6$	9671	(*b*)	0.645	9.658	8.795	5.294	107.42	429.06	2.025	2.9	41.9	2.415	1.627	1.4	13.7
$NaMnSi_2O_6$	62513	(*f*)	0.65	9.513	8.621	5.354	105.14	423.85	2.025	5.7	30.0	2.397	1.631	1.4	13.8
$NaTiSi_2O_6$	39194	(*g*)	0.67	9.692	8.874	5.301	106.85	436.35	2.046	2.4	28.5	2.422	1.627	1.3	17.3
$NaScSi_2O_6$	74553	(*h*)	0.73	9.8372	9.055	5.3488	107.175	455.2	2.102	2.7	35.3	2.453	1.631	1.8	13.6
$Na(In_{0.20}Sc_{0.80})Si_2O_6$	68749	(*i*)	0.742	9.8516	9.0698	5.3521	107.175	456.9	2.112	2.6	34.5	2.455	1.630	2.0	13.3
$Na(In_{0.40}Sc_{0.60})Si_2O_6$	68747	(*i*)	0.754	9.8634	9.0827	5.3542	107.174	458.28	2.119	2.5	34.4	2.456	1.630	1.9	12.0
$Na(In_{0.40}Sc_{0.60})Si_2O_6$	68748	(*i*)	0.754	9.8659	9.0848	5.3553	107.178	458.58	2.123	2.6	33.6	2.455	1.629	2.1	11.9
$Na(In_{0.50}Sc_{0.50})Si_2O_6$	68746	(*i*)	0.76	9.8701	9.0901	5.3559	107.179	459.09	2.121	2.5	34.8	2.457	1.631	1.8	11.3
$Na(In_{0.55}Sc_{0.45})Si_2O_6$	68745	(*i*)	0.763	9.8734	9.0947	5.3570	107.187	459.55	2.153	3.3	35.0	2.458	1.633	1.9	11.1
$Na(In_{0.60}Sc_{0.40})Si_2O_6$	68744	(*i*)	0.766	9.8782	9.101	5.3582	107.191	460.18	2.127	2.6	35.1	2.458	1.632	1.9	10.9
$Na(In_{0.65}Sc_{0.35})Si_2O_6$	68743	(*i*)	0.769	9.8811	9.1043	5.3592	107.188	460.59	2.128	2.4	34.8	2.459	1.631	1.9	11.0
$Na(In_{0.80}Sc_{0.20})Si_2O_6$	68742	(*i*)	0.778	9.8907	9.1164	5.3623	107.204	461.87	2.133	2.3	35.2	2.462	1.632	1.8	9.9
$NaInSi_2O_6$	2135	(*j*)	0.79	9.9023	9.1307	5.3589	107.201	462.86	2.141	2.2	34.4	2.457	1.632	1.9	10.1
$NaInSi2O_6$	68741	(*i*)	0.79	9.8997	9.1310	5.3656	107.226	463.26	2.141	2.2	35.0	2.460	1.632	2.1	9.8

Room-temperature data in all cases. References: (*a*) Prewitt & Burnham (1966); (*b*) Clark *et al.* (1969); (*c*) Ohashi *et al.* (1995); (*d*) Ohashi *et al.* (1983); (*e*) Ohashi *et al.* (1994*a*); (*f*) Ohashi *et al.* (1987); (*g*) Ohashi *et al.* (1982); (*h*) Ohashi *et al.* (1994*b*); (*i*) Ohashi *et al.* (1990); (*j*) Hawthorne & Grundy (1974). BLD = bond-length distortion (Renner & Lehmann 1986), OAV = octahedral angle variance (Toraya, 1981) and TAV = tetrahedral angle variance.

& Lehmann, 1986) is similar in the Al, Ga, V, Fe, Ti and Sc members (Fig. 2*b*) and decreases slightly towards the In^{3+} compound. Again the BLD for $NaTiSi_2O_6$ (2.7%) is in excellent agreement with the literature trend. The Mn compound is exceptional and exhibits strong bond-length distortion. This distortion is evidence for a stabilization of the Mn^{3+} in this pyroxene structure. The variation of the octahedral angle variance (OAV; Toraya, 1981) *versus* the ionic radius is depicted in Fig. 2(*c*). It decreases from the Al to the Sc member and remains constant towards In^{3+}. However, the Cr, V, Mn and Ti members deviate from this trend. The very same observation was made by Ohashi *et al.* (1987) when plotting the variation of the $M1-M1$ distance across the shared O1—O1 edge of the octahedral chain *versus* the averaged $M1$—O1 bond lengths. The shorter $M1-M1$ distances show a positive correlation with the smaller $M1$—O—$M1$ angles (Fig. 1 in Ohashi *et al.*, 1987), larger O1*a*1—$M1$—O1*b*2 angles and larger O1*a*2—$M1$—O1*b*2 angles (Fig. 2*d*). As the latter two angles are closer to the ideal values of 90 and 180°, respectively, this is one reason for the smaller octahedral angle variance in the Cr, V, Mn and Ti compounds and the fact that the octahedra appear to be more regular than in the Al, Ga, Fe, Sc and In members. The deviation of the Cr, Mn, V and Ti compounds from the other members of the $NaM^{3+}Si_2O_6$ series may be caused by the repulsion between the O1 atoms of the $M1$ site and the unpaired 3*d* electrons of the above transition metals.

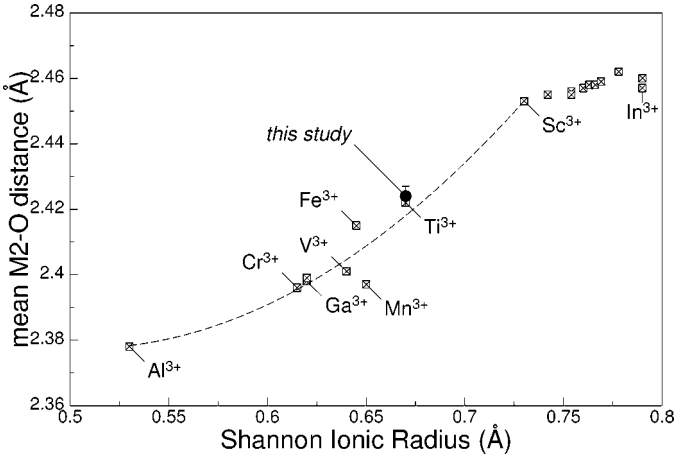

Figure 3
Average $M2$—O bond length (Å) *versus* the ionic radius of the $M1$ site cation for various $NaM^{3+}Si_2O_6$ clinopyroxenes. Structural references for individual compounds are given in Table 1. The regression line fitted to the data is a guide to the eye and serves to clarify trends. Error bars for the literature data are not shown, but are larger than the error bar for $NaTiSi_2O_6$, investigated in this study.

Within a coordination sphere of 2.6 Å, the $M2$ site is surrounded by six O atoms. Two further O3 atoms are 2.8–2.9 Å away from the sodium cation. Thus, sodium is sixfold coordinated, as was also found recently by Downs (2003) on the basis of procrystal electron density calculations. Increasing the size of the $M1$ cation also increases the individual and mean $M2$—O bond lengths (Fig. 3). The average $M2$—O bond length of 2.424 (2) Å found in this study for $NaTiSi_2O_6$ is in excellent agreement with the value calculated by Ohashi *et al.* (1982) and fits well into the literature trend. Changes in $M2$-site geometry are the result of changes within the $M1$ octahedra (Hawthorne & Grundy, 1977; Redhammer & Roth, 2003*a*).

As for the $M1$ and the $M2$ site, the mean tetrahedral Si—O bond length in $NaM^{3+}Si_2O_6$ clinopyroxenes depends on the size of the $M1$ site cation (Fig. 4*a*). With increasing $M1$ cation radius, the deviation of individual Si—O bond lengths from the average value (bond-length distortion, BLD) increases slightly (Fig. 4*b*). However, the BLD of the tetrahedron is

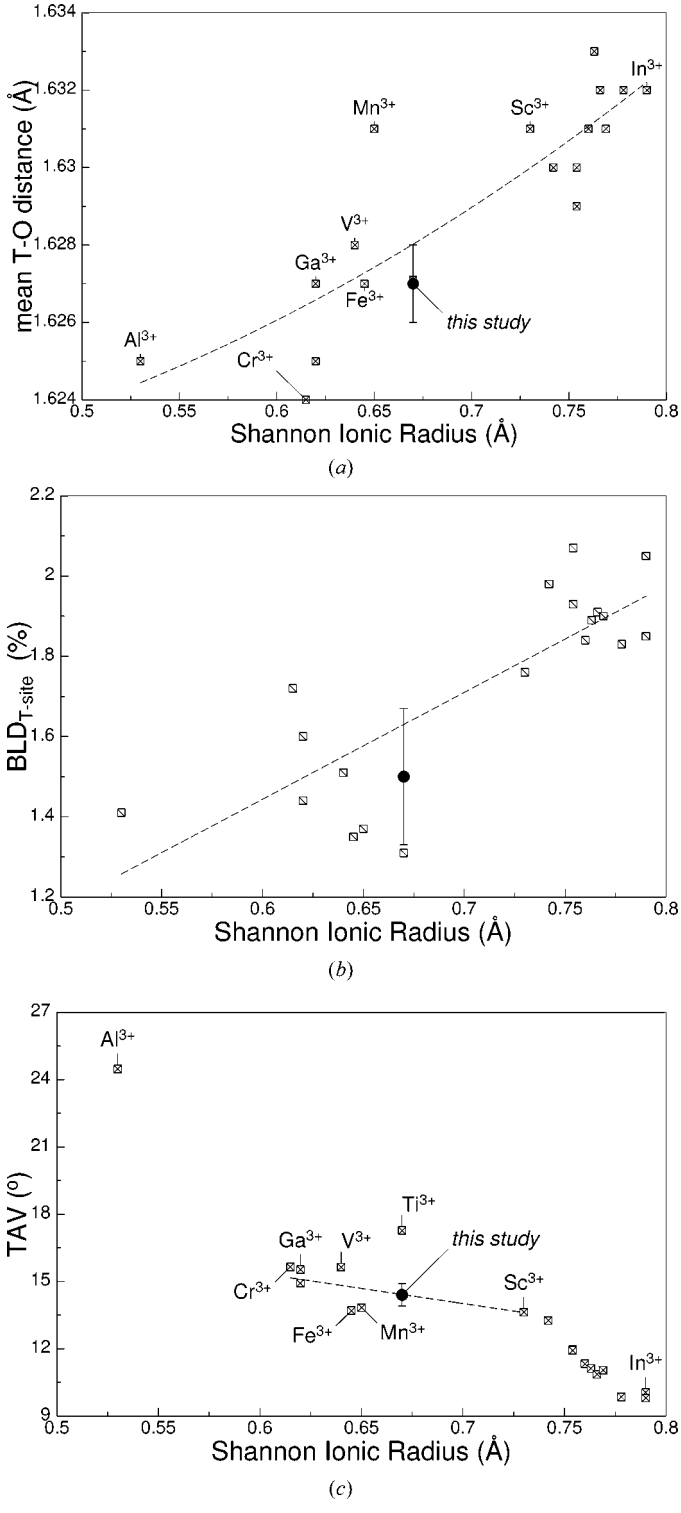

Figure 4
Derived structural parameters for the tetrahedral site for various $NaM^{3+}Si_2O_6$ clinopyroxenes. Structural references for individual compounds are given in Table 1. (*a*) Average Si—O bond length *versus* mean *M*1-site cationic radius; (*b*) bond-length distortion parameter, BLD (Renner & Lehmann, 1986), of the tetrahedron *versus* mean *M*1-site cationic radius; (*c*) quadratic tetrahedral angle variance, TAV (Toraya, 1981), *versus* mean *M*1-site cationic radius. The regression lines fitted to the data are guides to the eye and serve to clarify trends. Error bars for the literature data are not shown but are larger than the error bar for $NaTiSi_2O_6$, investigated in this study.

smaller than within the octahedral site. The tetrahedral angle variance (TAV), *i.e.* the quadratic deviation from the ideal value of 109.47°, is negatively correlated with the size of the *M*-site cation (Fig. 4*c*). No uniform trend can be deduced from the plot. The largest deviation from ideal tetrahedral geometry is found for $NaAlSi_2O_6$ with the smallest *M*1-site cation, the most ideal tetrahedron being that in $NaInSi_2O_6$ with the largest *M*1-site cation. Changes in the structural parameters within the tetrahedra are partly the result of the different space requirements between octahedral and tetrahedral chains and suggest that the stretching of the tetrahedral chains *via* variations in the O3—O3—O3 bridging angle is not sufficient to match the octahedral and the tetrahedral chain.

3.2. Structure determination and refinement at $T < 200$ K

Cooling $NaTiSi_2O6$ to 200 K does not change the symmetry. However, a dataset collected at 190 K showed pronounced splitting of some Bragg reflections, which disappeared rapidly when the temperature was raised above 197 K. The latter temperature is the proposed crystallographic phase transition

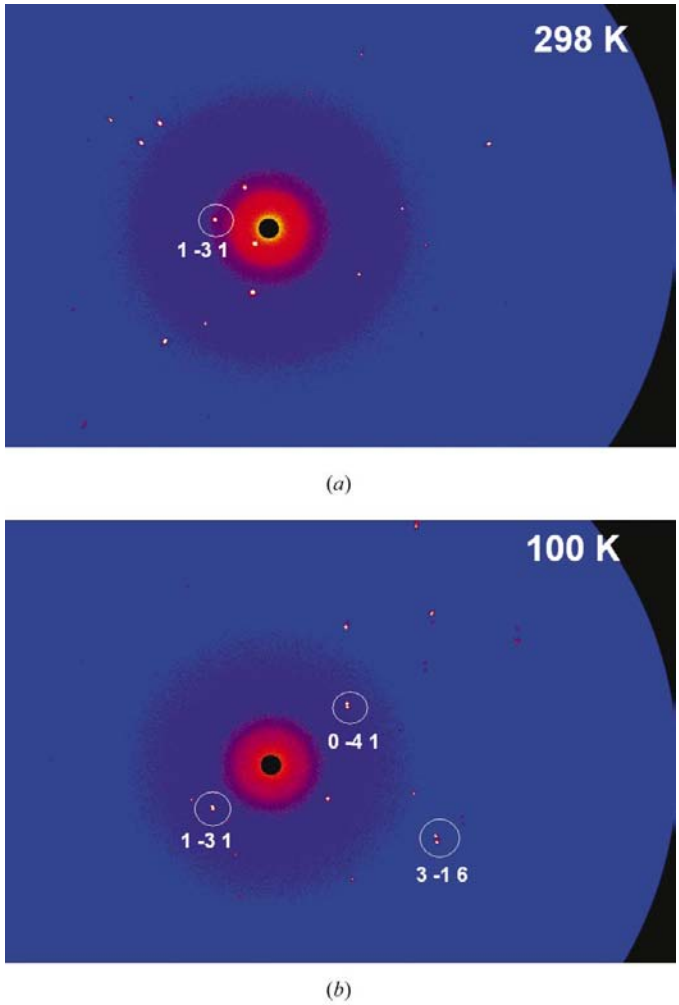

Figure 5
Image-plate diffraction frames of $NaTiSi_2O_6$, taken at (*a*) 298 and (*b*) 100 K, respectively, and both showing, among others, the $(13\bar{1})$ Bragg reflection.

Table 2
Lattice parameters for $NaTiSi_2O_6$ at different temperatures.

Temperature (K)	a (Å)	b (Å)	c (Å)	α (°)	β (°)	γ (°)	V (Å^3)
100	5.2967 (19)	6.5099 (20)	6.6153 (24)	84.59 (3)	77.73 (3)	77.76 (3)	217.54 (14)
110	5.2976 (18)	6.5159 (21)	6.6123 (20)	84.60 (3)	77.73 (3)	77.75 (3)	217.67 (12)
130	5.2976 (16)	6.5230 (20)	6.6073 (20)	84.63 (3)	77.72 (3)	77.75 (3)	217.74 (12)
140	5.2977 (16)	6.5273 (20)	6.6039 (20)	84.65 (3)	77.72 (3)	77.75 (3)	217.77 (12)
150	5.2988 (18)	6.5383 (20)	6.6021 (20)	84.66 (3)	77.70 (3)	77.76 (3)	218.12 (12)
160	5.2993 (16)	6.5396 (19)	6.5997 (22)	84.70 (3)	77.70 (3)	77.75 (3)	218.11 (12)
170	5.2989 (16)	6.5440 (19)	6.5960 (20)	84.74 (3)	77.70 (3)	77.74 (3)	218.12 (12)
180	5.2998 (16)	6.5521 (18)	6.5929 (20)	84.78 (3)	77.69 (3)	77.73 (3)	218.32 (12)
190	5.3019 (17)	6.5645 (19)	6.5891 (20)	84.83 (3)	77.69 (3)	77.71 (3)	218.68 (10)
200	9.7080 (26)	8.8718 (15)	5.3014 (14)	90	106.83 (2)	90	437.05 (19)
210	9.7069 (27)	8.8735 (17)	5.3023 (15)	90	106.83 (2)	90	437.16 (19)
215	9.7065 (27)	8.8746 (15)	5.3027 (14)	90	106.83 (2)	90	437.21 (19)
220	9.7052 (27)	8.8747 (17)	5.3029 (15)	90	106.84 (2)	90	437.17 (19)
240	9.7033 (27)	8.8774 (17)	5.3038 (15)	90	106.85 (2)	90	437.25 (19)
260	9.7017 (27)	8.8798 (17)	5.3045 (15)	90	106.84 (2)	90	437.39 (19)
298	9.6995 (30)	8.8833 (17)	5.3059 (14)	90	106.76 (2)	90	437.77 (20)

temperature. Fig. 5 shows portions of two image-plate diffraction pictures of $NaTiSi_2O_6$, collected at 298 and 100 K, respectively. Both show, among others, the $(13\bar{1})$ Bragg reflection. At 298 K the reflection appears as a sharp diffraction spot (Fig. 5*a*), whereas at 100 K it is split. On the frame collected at 100 K (Fig. 5*b*), the splitting is very prominent for the $(0\bar{4}1)$ and the $(3\bar{1}6)$ Bragg reflection. The splitting of Bragg reflections was identified as a twinning phenomenon. Below 200 K the intensity data could best be indexed using a primitive triclinic unit cell with lattice parameters a = 5.296 (2), b = 6.510 (2), c = 6.615 (2) Å, α = 84.59 (3), β = 77.73 (3) and γ = 77.76 (3)°. The unit-cell volume of the low-temperature structure is half that of the $C2/c$ high-temperature phase. The unit cell differs from that of Ninomiya *et al.* (2003) as we have chosen a cell with triclinic angles closer to 90°, however, the unit-cell volume of our data is similar to the value obtained by Ninomiya *et al.* (2003). The two twins are related to each other by the twin matrix (−1 0 0), (0 0 −1) (0−1 0). If a large detector-to-crystal distance (*e.g.* 180 mm) is chosen, the splitting of the two individuals is large enough for a separate integration of the diffraction pattern arising from the two individuals. Such measurements were performed at 100 and 180 K to define the twin matrix and to develop a structural model for the low-temperature phase. However, the overlap of the Bragg reflections (∼ 50% of the observed data) is large and the number of available reflection data is limited. Thus, for structure refinement we decided to use a small detector-to-crystal distance (60–80 mm), to integrate the Bragg reflections arising from the two twin individuals together by using large integration spots and to use the TWIN and BASF instructions as implemented in *SHELXL*97 (Sheldrick 1997*b*). A full absorption correction was performed for data sets between 200 and 298 K (monoclinic phase), but no reasonable correction was possible for the twin data sets of the triclinic phase (100–190 K).

The low-temperature structure was solved in the space group $P\bar{1}$ and refined to final a R_1 value < 0.025 and a final wR_2 value < 0.050 for all measurements in the temperature range 100–190 K. In the low-temperature structure, there is one symmetry-independent sodium position, one titanium position, two different silicon and six different O-atom positions. Despite the changes in symmetry and the size of the unit cell, the general structural topology does not change very much. In Fig. 6 the structure of $NaTiSi_2O_6$ at 100 K is displayed in a view down the [011] direction and is similar to that viewed in Fig. 1. Except for the Na atom, it was not possible to refine the atomic displacement parameters in their anisotropic form as the thermal parameter matrices became non-positive definite. This may be due to the fact that it was not possible to perform a reasonable absorption correction for the triclinic phase and/or this may also be an artefact of the integration of the intensity data arising from the two twin individuals. Table 2 compiles the lattice parameters between 298 and 100 K, and Table 3 gives experimental details on structure refinement at selected temperatures.[1] Finally, selected geometric and distortion parameters of $NaTiSi_2O_6$ are compiled in Table 4.

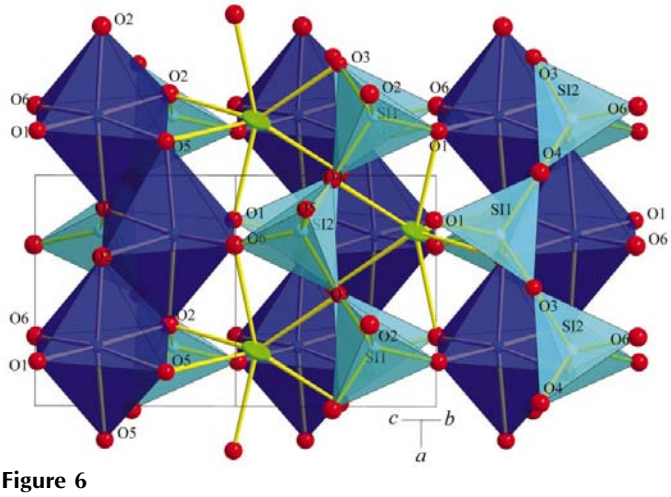

Figure 6
Structure of $NaTiSi_2O_6$ at 100 K in a projection along [011].

[1] Supplementary data for this paper are available from the IUCr electronic archives (Reference: WS5001). Services for accessing these data are described at the back of the journal.

Table 3
Experimental details of $NaTiSi_2O_6$ at selected temperatures.

Data sets have been collected at 100, 110, 130, 140, 150, 160, 170, 180, 190, 200, 210, 215, 220, 240, 260 and 298 K. Full data can be obtained from the cif which has been deposited.

	260	200	190	130	100
Crystal data					
Chemical formula	O_6NaSi_2Ti	O_6NaSi_2Ti	O_6NaSi_2Ti	O_6NaSi_2Ti	O_6NaSi_2Ti
M_r	223.07	223.07	223.07	223.07	223.07
Cell setting, space group	Monoclinic, $C2/c$	Monoclinic, $C2/c$	Triclinic, $P\bar{1}$	Triclinic, $P\bar{1}$	Triclinic, $P\bar{1}$
a, b, c (Å)	9.702 (3), 8.8798 (17), 5.3045 (15)	9.708 (3), 8.8718 (15), 5.3014 (14)	5.3019 (16), 6.5645 (19), 6.589 (2)	5.2976 (16), 6.523 (2), 6.607 (2)	5.2967 (19), 6.510 (2), 6.615 (2)
α, β, γ (°)	90, 106.83 (2), 90	90, 106.83 (2), 90	84.83 (2), 77.69 (2), 77.71 (2)	84.63 (3), 77.72 (2), 77.75 (2)	84.59 (3), 77.73 (3), 77.76 (3)
V (Å^3)	437.39 (19)	437.05 (18)	218.68 (11)	217.74 (11)	217.54 (13)
Z	4	4	2	2	2
D_x (Mg m^{-3})	3.387	3.39	3.388	3.402	3.406
Radiation type	Mo $K\alpha$	Mo $K\alpha$	Mo $K\alpha$	Mo $K\alpha$	Mo $K\alpha$
No. of reflections for cell parameters	2950	2123	1911	2033	1586
θ range (°)	2.1–2.3	2.1–2.9	2.1–2.3	2.1–2.3	2.1–2.3
μ (mm^{-1})	2.55	2.55	2.55	2.56	2.57
Temperature (K)	260 (1)	200 (1)	190 (1)	130 (1)	100 (1)
Crystal form, colour	Prismatic, blue	Prismatic, blue	Prismatic, blue	Prismatic, blue	Prismatic, blue
Crystal size (mm)	0.17 × 0.10 × 0.08	0.17 × 0.10 × 0.08	0.17 × 0.10 × 0.08	0.17 × 0.10 × 0.08	0.17 × 0.10 × 0.08
Data collection					
Diffractometer	STOE IPDS 2	STOE IPDS 2	STOE IPDS 2	STOE IPDS 2	STOE IPDS 2
Data collection method	Rotation method	Rotation method	Rotation method	Rotation method	Rotation method
Absorption correction	Empirical (using intensity measurements)	Empirical (using intensity measurements)	None	None	None
T_{min}	0.642	0.632	–	–	–
T_{max}	0.729	0.748	–	–	–
No. of measured, independent and observed reflections	2033, 710, 633	2329, 671, 589	1514, 814, 673	1278, 687, 588	1030, 663, 564
Criterion for observed reflections	$I > 2\sigma(I)$	$I > 2\sigma(I)$	$I > 2\sigma(I)$	$I > 2\sigma(I)$	$I > 2\sigma(I)$
R_{int}	0.026	0.027	0.033	0.032	0.022
θ_{max} (°)	32.0	31.7	26.4	24.7	24.7
Range of h, k, l	$-13 \rightarrow h \rightarrow 11$ $-11 \rightarrow k \rightarrow 13$ $-7 \rightarrow l \rightarrow 7$	$-14 \rightarrow h \rightarrow 14$ $-11 \rightarrow k \rightarrow 11$ $-7 \rightarrow l \rightarrow 7$	$-6 \rightarrow h \rightarrow 6$ $-7 \rightarrow k \rightarrow 8$ $-8 \rightarrow l \rightarrow 8$	$-6 \rightarrow h \rightarrow 6$ $-7 \rightarrow k \rightarrow 7$ $-7 \rightarrow l \rightarrow 7$	$-6 \rightarrow h \rightarrow 6$ $-7 \rightarrow k \rightarrow 7$ $-7 \rightarrow l \rightarrow 6$
Refinement					
Refinement on	F^2	F^2	F^2	F^2	F^2
$R[F^2 > 2\sigma(F^2)]$, $wR(F^2)$, S	0.018, 0.045, 1.15	0.021, 0.047, 1.21	0.028, 0.055, 1.14	0.026, 0.053, 1.12	0.029, 0.073, 1.09
No. of reflections	710	671	814	687	663
No. of parameters	48	48	48	48	48
Weighting scheme	$w = 1/[\sigma^2(F_o^2) + (0.0226P)^2 + 0.165P]$, where $P = (F_o^2 + 2F_c^2)/3$	$w = 1/[\sigma^2(F_o^2) + (0.0238P)^2]$, where $P = (F_o^2 + 2F_c^2)/3$	$w = 1/[\sigma^2(F_o^2) + (0.0154P)^2 + 0.2991P]$, where $P = (F_o^2 + 2F_c^2)/3$	$w = 1/[\sigma^2(F_o^2) + (0.0153P)^2 + 0.3749P]$, where $P = (F_o^2 + 2F_c^2)/3$	$w = 1/[\sigma^2(F_o^2) + (0.0396P)^2 + 0.2805P]$, where $P = (F_o^2 + 2F_c^2)/3$
$(\Delta/\sigma)_{max}$	<0.0001	<0.0001	<0.0001	<0.0001	<0.0001
$\Delta\rho_{max}$, $\Delta\rho_{min}$ (e Å^{-3}	0.43, −0.43	0.32, −0.39	0.45, −0.39	0.33, −0.47	0.42, −0.62
Extinction method	*SHELXL*	*SHELXL*	None	None	None
Extinction coefficient	0.0238 (14)	0.0132 (16)	–	–	–

Computer programs used: Stoe *X-AREA* (Stoe & Cie, 2002), *SHELXS*97 (Sheldrick, 1997*a*), *SHELXL*97 (Sheldrick, 1997*b*).

3.3. Structural variation with temperature

3.3.1. Unit-cell parameters. Fig. 7 displays the changes in unit-cell parameters as a function of temperature. To clarify temperature variations and to ease discussion, the triclinic unit cell was transformed in such a way that it was comparable to that of the high-temperature monoclinic cell with the transformation matrix (0 −1 −1) (0 1−1) (1 0 0). Within the monoclinic $C2/c$ phase, the unit-cell parameter a increases by 0.09% with decreasing temperature and remains constant in the triclinic phase below 200 K (Fig. 7*a*). The cell parameters b (Fig. 7*b*) and c (Fig. 7*c*) decrease with decreasing temperature, both in the monoclinic and in the triclinic phase, however, with different slopes. Within the $C2/c$ phase the c parameter decreases by about the same amount (0.09%) with decreasing

Table 4
Selected bond lengths (Å), bond angles (°) and polyhedral distortion parameters for $NaTiSi_2O_6$ at different temperatures (atom identifiers in the monoclinic symmetry in parentheses).

Temperature (K)	100	130	150	170	190	200	220	240	260	298
*M*2 polyhedron										
Na—O1 (O2)	2.360 (5)	2.371 (6)	2.372 (5)	2.374 (5)	2.385 (5)	2.408 (1)	2.409 (1)	2.409 (1)	2.410 (1)	2.414 (1)
Na—O6 (O2)	2.457 (5)	2.452 (5)	2.449 (5)	2.450 (5)	2.440 (5)	2.408 (1)	2.409 (1)	2.409 (1)	2.410 (1)	2.414 (1)
Na—O2 (O1) (Å)	2.396 (5)	2.404 (6)	2.414 (5)	2.415 (4)	2.430 (5)	2.418 (1)	2.418 (1)	2.419 (1)	2.420 (1)	2.422 (1)
Na—O5 (O1) (Å)	2.420 (5)	2.419 (5)	2.411 (5)	2.415 (5)	2.406 (5)	2.418 (1)	2.418 (1)	2.419 (1)	2.420 (1)	2.422 (1)
Na—O3 (O3) (Å)	2.416 (5)	2.416 (6)	2.420 (5)	2.418 (5)	2.436 (6)	2.436 (1)	2.437 (1)	2.436 (1)	2.436 (1)	2.437 (1)
Na—O4 (O3) (Å)	2.445 (6)	2.445 (6)	2.450 (5)	2.444 (5)	2.440 (6)	2.436 (1)	2.437 (1)	2.436 (1)	2.436 (1)	2.437 (1)
Na—O4 (O3) (Å)	2.769 (5)	2.774 (6)	2.781 (5)	2.786 (5)	2.802 (6)	2.839 (1)	2.840 (1)	2.840 (1)	2.841 (1)	2.841 (1)
Na—O3 (O3) (Å)	2.896 (5)	2.892 (6)	2.890 (5)	2.885 (5)	2.877 (6)	2.839 (1)	2.840 (1)	2.840 (1)	2.841 (1)	2.841 (1)
$\langle Na—O\rangle_6$	2.416	2.418	2.419	2.419	2.423	2.420	2.421	2.421	2.422	2.424
BLD_6 (%)	0.33	0.27	0.24	0.24	0.16	0.11	0.10	0.10	0.10	0.08
*M*1 octahedron										
Ti—O2 ($O1_{apex}$)	2.052 (5)	2.051 (5)	2.053 (4)	2.054 (4)	2.051 (5)	2.085 (1)	2.083 (1)	2.083 (1)	2.083 (1)	2.085 (1)
Ti—O5 ($O1_{apex}$)	2.126 (5)	2.128 (5)	2.126 (4)	2.124 (4)	2.124 (5)	2.085 (1)	2.083 (1)	2.083 (1)	2.083 (1)	2.085 (1)
Ti—O6 (O2)	1.943 (5)	1.951 (5)	1.951 (4)	1.951 (4)	1.961 (4)	1.971 (1)	1.970 (1)	1.970 (1)	1.969 (1)	1.969 (1)
Ti—O1 (O2) (Å)	1.995 (5)	1.985 (5)	1.990 (4)	1.990 (4)	1.985 (5)	1.971 (1)	1.970 (1)	1.970 (1)	1.969 (1)	1.969 (1)
Ti—O2 (O1)	2.112 (5)	2.111 (5)	2.099 (4)	2.106 (4)	2.099 (5)	2.102 (1)	2.105 (1)	2.105 (1)	2.106 (1)	2.107 (1)
Ti—O5 (O1)	2.074 (4)	2.082 (5)	2.094 (4)	2.091 (4)	2.105 (4)	2.102 (1)	2.105 (1)	2.105 (1)	2.106 (1)	2.107 (1)
$\langle M1—O\rangle$ (Å)	2.050	2.051	2.052	2.053	2.054	2.052	2.052	2.052	2.053	2.054
$\langle Ti—O_{(equat.)}\rangle$	2.031	2.032	2.034	2.034	2.038	2.036	2.037	2.037	2.038	2.038
$\langle Ti—O_{(apex)}\rangle$	2.089	2.090	2.090	2.089	2.087	2.085	2.083	2.083	2.083	2.085
BLD (%)	0.34	0.40	0.48	0.45	0.55	0.54	0.56	0.56	0.57	0.57
OAV (°)	26.00	25.53	25.85	26.52	26.38	26.03	26.54	26.78	27.03	27.41
Ti—Ti	3.071 (3)	3.079 (3)	3.082 (3)	3.089 (3)	3.110 (3)	3.166 (1)	3.169 (1)	3.170 (1)	3.172 (1)	3.175 (1)
Ti—Ti	3.225 (3)	3.222 (3)	3.225 (3)	3.227 (3)	3.217 (3)	–	–	–	–	
Ti—O2—Ti	95.0 (2)	95.4 (2)	95.8 (2)	95.9 (2)	97.1 (2)	98.26 (8)	98.34 (7)	98.41 (8)	98.45 (6)	98.46 (7)
Ti—O5—Ti	100.3 (1)	99.9 (2)	99.7 (2)	99.9 (2)	99.1 (2)	–	–	–	–	–
Si1 tetrahedron										
Si1—O1 (O2)	1.596 (5)	1.593 (5)	1.592 (5)	1.588 (4)	1.589 (5)	1.594 (1)	1.596 (1)	1.595 (1)	1.596 (1)	1.595 (1)
Si1—O2 (O1)	1.624 (5)	1.626 (5)	1.633 (5)	1.627 (4)	1.636 (5)	1.630 (1)	1.629 (1)	1.629 (1)	1.628 (1)	1.628 (1)
Si1—O3 (O3)	1.649 (4)	1.646 (4)	1.653 (4)	1.648 (4)	1.645 (4)	1.640 (1)	1.640 (1)	1.641 (1)	1.640 (1)	1.640 (1)
Si1—O4 (O3)	1.653 (4)	1.652 (4)	1.655 (4)	1.657 (4)	1.651 (4)	1.648 (1)	1.648 (1)	1.647 (1)	1.646 (1)	1.647 (1)
⟨Si1—O⟩	1.631	1.629	1.633	1.630	1.630	1.628	1.628	1.628	1.628	1.627
⟨Si—O(br)⟩	1.651	1.649	1.654	1.652	1.648	1.644	1.644	1.644	1.643	1.643
⟨Si—O(nbr)⟩	1.610	1.609	1.612	1.607	1.613	1.612	1.612	1.612	1.612	1.611
BLD (%)	1.26	1.21	1.29	1.39	1.26	1.04	0.99	1.01	0.97	1.00
TAV (°)	19.03	19.91	19.69	18.09	17.48	14.62	14.28	14.41	14.49	14.49
Si—O3—Si (°)	139.8 (2)	139.8 (2)	139.8 (2)	139.8 (3)	139.8 (2)	139.9 (6)	139.92 (7)	139.88 (6)	139.94 (8)	140.01 (6)
Si—O4—Si (°)	139.7 (2)	139.9 (2)	134.0 (3)	139.7 (3)	140.1 (3)	–	–	–	–	–
O3—O4—O3	173.8 (2)	173.8 (2)	173.7 (2)	173.7 (2)	173.7 (2)	173.67 (6)	173.72 (6)	173.81 (8)	173.9 (7)	173.99 (6)
Si2 tetrahedron										
Si2—O6	1.587 (5)	1.598 (5)	1.600 (5)	1.602 (4)	1.602 (4)	–	–	–	–	–
Si2—O5	1.629 (5)	1.623 (5)	1.621 (5)	1.626 (4)	1.619 (5)	–	–	–	–	–
Si2—O4	1.636 (4)	1.636 (4)	1.628 (4)	1.630 (4)	1.634 (4)	–	–	–	–	–
Si2—O3	1.640 (4)	1.640 (4)	1.638 (4)	1.642 (4)	1.646 (4)	–	–	–	–	–
⟨Si—O⟩	1.623	1.624	1.622	1.625	1.625	–	–	–	–	–
⟨Si—O(br)⟩	1.638	1.638	1.633	1.636	1.640	–	–	–	–	–
⟨Si—O(nbr)⟩	1.608	1.611	1.611	1.614	1.610	–	–	–	–	–
BLD (%)	1.11	0.86	0.70	0.72	0.93	–	–	–	–	–
TAV (°)	13.04	11.88	12.46	13.10	11.90	–	–	–	–	–

temperature as *a* increases, whereas *b* deceases by 0.13% with decreasing temperature. The change in *b* below 200 K significantly deviates from linearity. As for the monoclinic *C*2/*c* phase, the most significant temperature-dependent variations within the triclinic $P\bar{1}$ phase concern the (transformed) *b* cell parameter. The latter changes by 0.44% (0.02% for the *a* and 0.09% for the *c* unit-cell parameters). Transformed to the monoclinic-like cell, between 298 and 100 K, the α angle changes from 90 to 90.16°. The γ angle, however, evolves towards 89° between 200 and 100 K and thus distinctly departs from 90° (Fig. 7*d*). Excluding the data point at 298 K, the monoclinic β angle shows a slight decrease within the *C*2/*c* phase and uniformly decreases in the triclinic phase with decreasing temperature (Fig. 7*e*). The present results on the different monoclinic β angle at room temperature between this study and the data from Ohashi *et al.* (1982) are consistent with the discussion on quenchability (Ohashi, 2003). That is, the quenching conditions affect the β angle in $NaTiSi_2O_6$ and

hard quenching results on a larger β angle. This is supported by the fact that the monoclinic angle of the crystal we have used (kept at 1 atm for 21 years) and that of Ninomiya *et al.* (2003) are of similar size.

3.3.2. The octahedral *M*1 (Ti^{3+}) site. In the triclinic low-temperature form there are six different Ti^{3+}—O distances ranging from 1.943 (5) to 2.126 (4) Å (at 100 K). The mean Ti^{3+}—O bond length is 2.053 Å at this temperature. Increasing

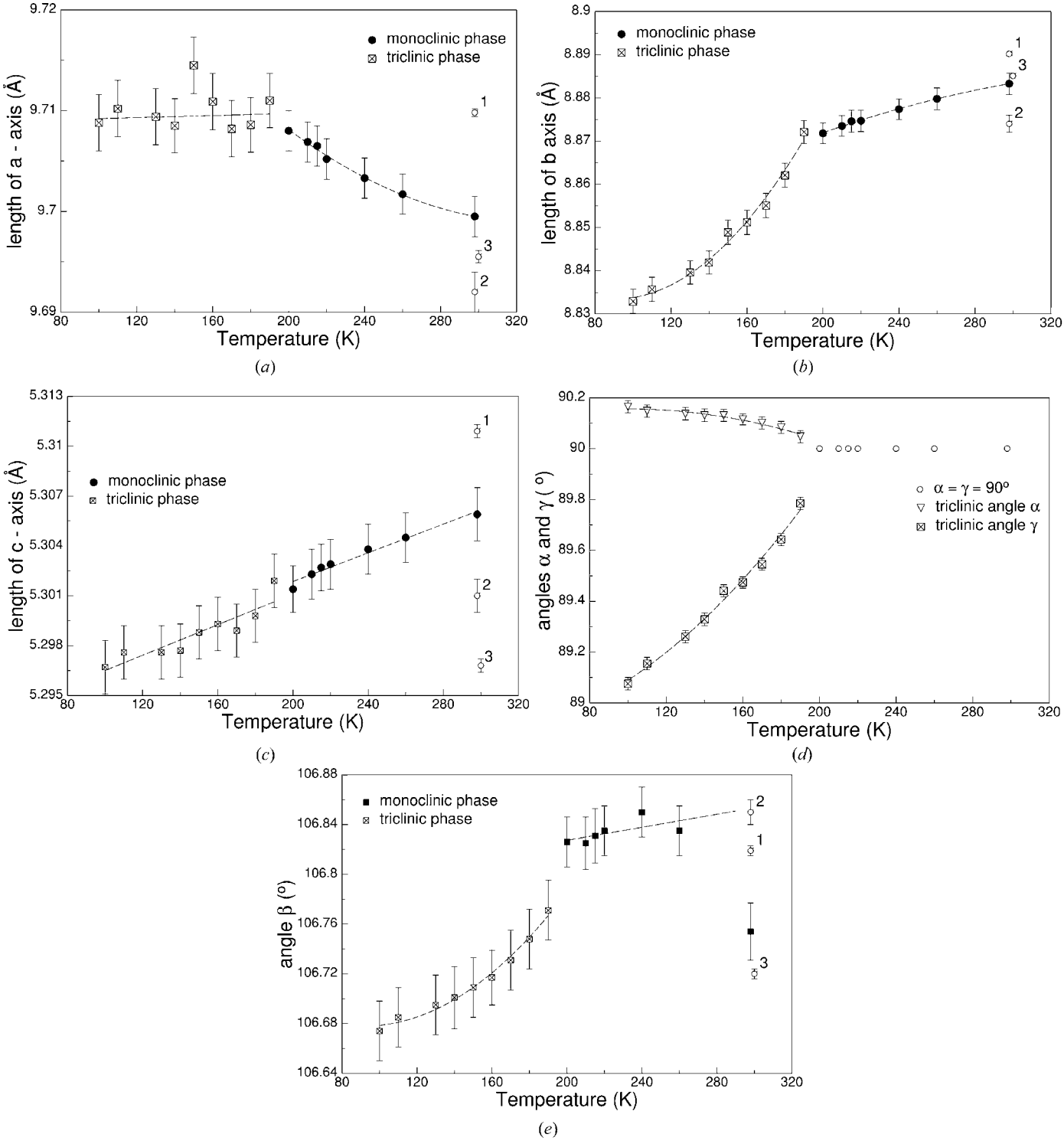

Figure 7
Unit-cell parameters of $NaTiSi_2O_6$ as a function of temperature. To ease the comparison between *C*2/*c* and $P\bar{1}$ data, the low-temperature phase data ($T <$ 200 K) were transformed to a pseudo-monoclinic cell using the transformation matrix (0 −1 −1), (0 1 −1) and (1 0 0). The regression lines fitted to the data are guides to the eye and serve to clarify trends; 1 = literature data from Ohashi (2003), 2 = literature data from Ohashi *et al.* (1982), 3 = literature data from Ninomiya *et al.* (2003).

the temperature slightly increases the average Ti—O bond length by ~ 0.004 Å (Fig. 8*a*). The phase transition is marked by a discontinuous variation in the mean Ti—O bond length, which slightly increases with temperature in the *C*2/*c* phase, however, with a different slope. The *C*2/*c* → $P\bar{1}$ phase transition is associated with marked alterations of the individual Ti^{3+}—O bond lengths. The bonds from Ti^{3+} to the apex O atoms (O1*a*2,*b*2 atoms in *C*2/*c*), which are identical above 190 K, split up into two distinctly different bond lengths: one short and one long Ti^{3+}—O_{apex} bond length (Fig. 8*b*). The difference between the two Ti^{3+}—O_{apex} bond lengths ranges between 0.070 and 0.077 Å. The long Ti^{3+}—O_{apex} bond length tends to increase with decreasing temperature down to ~160 K and decreases thereafter. Within the equatorial plane of the octahedron, the bond lengths between Ti^{3+} and the O2 atoms (*C*2/*c* phase) slightly increase with decreasing temperature, a trend which is opposite to what is expected. Again, at the phase transition the two Ti^{3+}—O2 bond lengths, identical in *C*2/*c*, split up into two different lengths in $P\bar{1}$. The Ti^{3+}—O1 bond length increases and the Ti^{3+}—O6 bond length decreases with decreasing temperature (Fig. 8*c*). The differences between the Ti^{3+}—O1 and Ti^{3+}—O6 bond lengths increase from 0.024 (190 K) to 0.052 Å (100 K). The bonds displayed in Fig. 8(*c*) connect the linear chain of TiO_6 octahedra laterally with the SiO_4 tetrahedral chains. The smallest changes within the *M*1 octahedron during temperature reduction are observed for the bonds connecting Ti^{3+} with the equatorial O1 atom (in the *C*2/*c* phase) and the O2 and O5 atoms, respectively (in the $P\bar{1}$ phase) (Fig. 8*d*). These are the O atoms which connect the octahedral chain vertically ([1 0 0] direction in *C*2/*c*, [0 1 1] direction in $P\bar{1}$) to the tetrahedral chains. Although the difference between the two individual bond lengths Ti—O2 and Ti—O5 increases with decreasing temperature (0.006 Å at 190 K and 0.038 Å at 100 K), there is no large jump between the data at 190 and 200 K, as observed especially for the Ti—O_{apex} bond lengths (Fig. 8*b*). All the above changes in bond lengths can be understood in the light of one of the most evident changes upon the phase transition, namely the shortest distances between neighbouring Ti^{3+}–Ti^{3+} cations. At room temperature, the Ti^{3+}—Ti^{3+} distance is 3.175 (1) Å and decreases almost linearly to 3.166 (1) Å at 200 K (Fig. 9*a*). In the triclinic phase, however, two indepen-

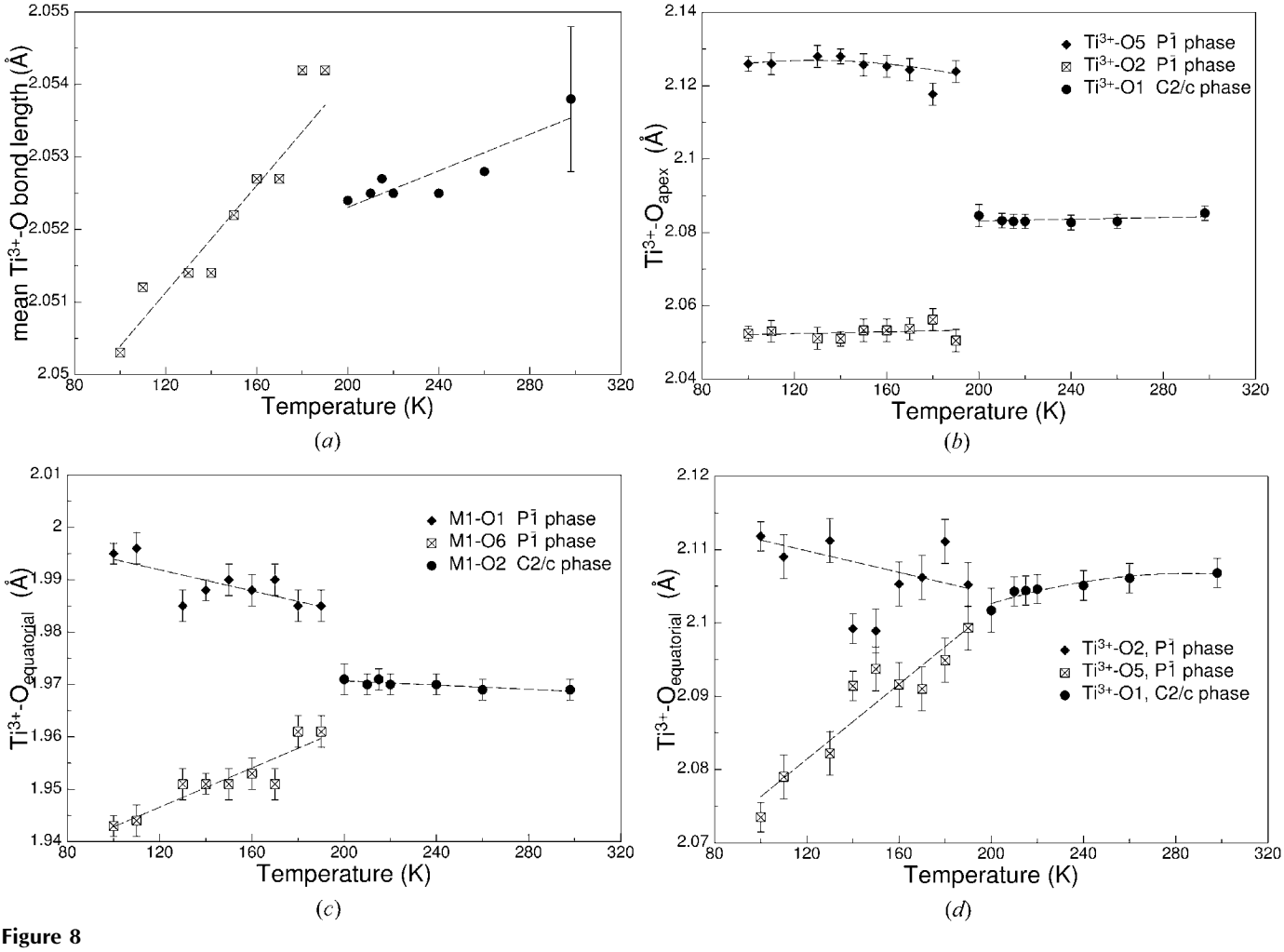

Figure 8
(*a*) Mean and (*b*)–(*d*) individual *M*1—O bond lengths plotted as a function of temperature. Regression lines, fitted to the data, are guides to the eye and serve to clarify trends. Error bars in Fig. 8(*a*) are only shown for one datapoint to keep the figure clear. All other error bars are of similar size to that shown.

dent sets of Ti—Ti distances do exist, a short one of 3.071 (1) Å and a longer one of 3.225 (1) Å (at 100 K). At a temperature of 190 K, the two Ti—Ti distances still differ by as much as 0.107 Å. As a consequence of the two sets of Ti—Ti distances, two different sets of Ti—O—Ti angles also exist (Fig. 9*b*). Within the *M*1 octahedron, the Ti—O distances within the equatorial plane of the octahedron are distinctly smaller compared with those from Ti^{3+} to the apex O atoms of

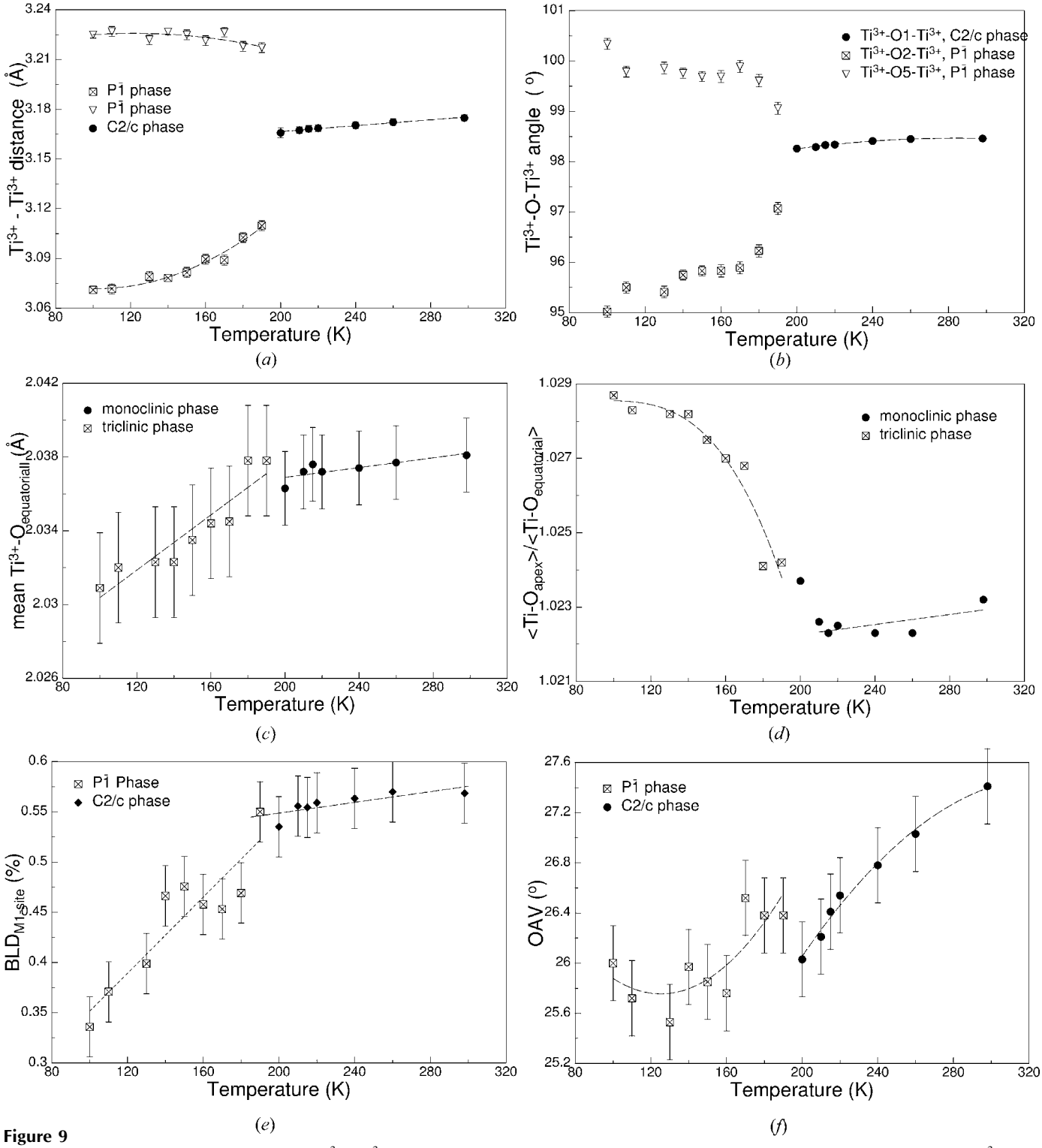

Figure 9
Temperature-dependent alteration of (*a*) the Ti^{3+}—Ti^{3+} interatomic distance within the *M*1 octahedral chain; (*b*) the interatomic bond angle Ti^{3+}—O—Ti^{3+}; (*c*) the mean Ti^{3+}—O bond length within the equatorial plane of the octahedron; (*d*) the quotient between the average Ti^{3+}–O bond lengths within the equatorial plane and the mean bond lengths from Ti^{3+} to the two apex O atoms of the *M*1 octahedron; (*e*) the bond-length distortion parameter, BLD (Renner & Lehmann, 1986); (*f*) the quadratic, octahedral angle variance, and for $NaTiSi_2O_6$. Regression lines fitted to the data are guides to the eye and serve to clarify trends. Error bars, if not visible, are smaller than the symbols.

the octahedron. Thus, the *M*1 site appears to be tetragonally stretched in the chain direction. The average of the Ti—O_{apex} bond lengths is slightly larger in the $P\bar{1}$ phase than in the *C*2/*c* phase. The average of the Ti—$O_{equatorial}$ bond lengths remains almost constant with decreasing temperature within the *C*2/*c* phase, but decreases more distinctly in the $P\bar{1}$ phase (Fig. 9*c*). Altogether, this behaviour gives a rather constant degree of tetragonal stretching between 298 and 200 K (*C*2/*c*), but an increased stretching in the chain direction with decreasing temperature in the triclinic phase (Fig. 9*d*). Although the TiO_6 octahedra become more stretched at low temperatures, they appear to be slightly more ideal (*i.e.* closer to the geometry of an ideal octahedron) at low temperatures. This is reflected by the decrease of both the bond-length distortion parameter (Fig. 9*e*) and the smaller values of the quadratic octahedral-angle variance (Fig. 9*f*).

The geometry of the *M*1 site can be characterized by plotting the *M*1—*M*1 (Ti^{3+}—Ti^{3+}) interatomic distance *versus* the mean M1—O1 distance (for the *C*2/*c* phase). These are the bonds pointing from the *M*1 (Ti^{3+}) cation to the two O1 atoms, forming the common edge between neighbouring *M*1 octahedra. In $P\bar{1}$ the mean *M*1—O bonds, corresponding to the *M*1—O1 bonds in *C*2/*c*, are the mean Ti—O2 and the mean Ti—O5 bonds (Fig. 1, Fig. 6). In Fig. 10, data points for compounds having spherical M^{3+} cations [Al^{3+}, Ga^{3+} ($3d^0$), Fe^{3+} ($3d^5$), Sc^{3+} and In^{3+}] are plotted onto one common, nearly linear trend. Data for the atoms with a non-spherical electron configuration [Cr^{3+} ($3d^3$), V^{3+} ($3d^2$), Mn^{3+} ($3d^4$) and Ti^{3+} ($3d^1$)], however, distinctly fall off the trend. The data for $NaTiSi_2O_6$ in the *C*2/*c* phase agree well with the recent results of Ohashi (2003); both distinctly deviate from the spherical atom region. With decreasing temperature, data deviate even more from the trend defined by the Al–Ga–Fe–Sc–In series. For the $P\bar{1}$ phase, the data points, representing the longer Ti^{3+}—Ti^{3+} distance and the mean Ti—O5 bond length, can be plotted onto the spherical atom region. On the other hand, the data points representing the shorter Ti—Ti distance and the mean Ti—O2 bond length distinctly fall off this trend. This suggests that the one t_{2g} electron of Ti^{3+} is localized towards the O2 atom. Similar relationships can be deduced for the Ti—O—Ti angles. In the $P\bar{1}$ phase, the larger Ti^{3+}—O5—Ti^{3+} angle corresponds to the spherical atom region. That means that the localization of the one t_{2g} *d*-electron of $NaTiSi_2O_6$ shows a unique correlation between the mean Ti—O2 (Ti—O2/Ti—O5 in $P\bar{1}$) bond lengths and the Ti—Ti and/or the Ti—O—Ti interatomic distance/bond angle.

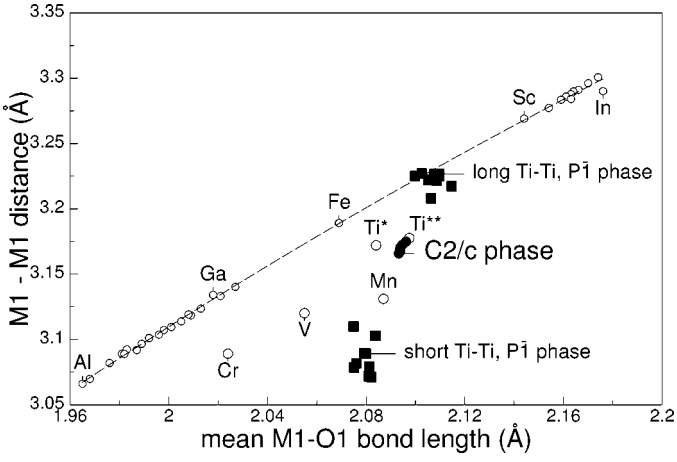

Figure 10
Variation of the *M*1—*M*1 interatomic distance *versus* the mean of the *M*1—O bond lengths (in *C*2/*c*) for various $NaM^{3+}Si_2O_6$ clinopyroxenes. Open circles represent literature data and references for them are given in Table 1. Additionally, data for the series $Na(Al,Ga)Si_2O_6$ from Ohashi (2003) have been added. The label Ti* represents the datapoint for $NaTiSi_2O_6$ from Ohashi *et al.* (1982) and Ti** that for $NaTiSi_2O_6$ from Ohashi (2003). Filled symbols represent the data of this study.

3.3.3. The *M*2 site. Sodium is sixfold coordinated in both the triclinic and the monoclinic phase. Within the *C*2/*c* phase the Na—O bond lengths decrease with decreasing temperature. The largest decrease is shown by the Na—O2 bond length which changes by 0.25% between 298 and 200 K (Fig. 11*a*). As the Ti—O2 bond lengths increase slightly with decreasing temperature, this suggests that the O2 atoms move towards the sodium cation. The Na—O1 bond lengths decrease by 0.17% between 298 and 200 K (Fig. 11*b*), whereas the Na—O3 distances remain almost constant (vary only 0.04%, Fig. 11*c*). As for the Ti—O bond lengths, the *C*2/*c* → $P\bar{1}$ phase transition is again associated with some marked jumps in the temperature-dependent variation of the Na—O bond lengths. While the *C*2/*c* phase has three different Na—O bonds, there are six in the triclinic low-temperature structure. The jumps in the size of the Na—O1 and Na—O6 bond lengths upon the phase transition are directly related to the discontinuous alterations of the Ti—O bond lengths. The O6 atom is moved closer to Ti^{3+} (shrinkage of the Ti—O6 bond, Fig. 8*c*) and, consequently, the Na—O6 bond length increases (Fig. 11*a*). The opposite argument applies to the Ti—O1 and the Na—O1 bond lengths. In the triclinic phase the Na—O2 and the Na—O5 bond lengths (Fig. 11*b*) show less pronounced changes with temperature. This again correlates well with the behaviour of the Ti—O2 and Ti—O5 bond lengths (Fig. 8*d*). The Na—O3 and the Na—O4 bond lengths (Fig. 11*c*) link the *M*2 site with the tetrahedral chain. For the latter bonds a slight decrease can be noted with decreasing temperature within the triclinic phase. The difference between the two bonds is ∼ 0.035 Å close to the phase transition and reduced somewhat to 0.030 Å at 100 K. The rapid changes of the bond lengths Na—O3 and Na—O4 suggest some pronounced variations in the geometry of the tetrahedral chain(s). The average Na—O bond lengths (Fig. 11*d*) decrease both in the monoclinic and in the triclinic phase with almost the same slope. However, the average Na—O bond length does not reflect the different alterations within the Na-coordination sphere, which are mainly forced by the changes in the *M*1-site geometry.

3.3.4. The tetrahedral site. The *C*2/*c* → $P\bar{1}$ phase transition results in two symmetrically non-equivalent Si-atom positions, causing two different SiO_4 tetrahedra, $Si(1)O_4$ and $Si(2)O_4$, which alternate within one tetrahedral chain (Fig. 6). This contrasts the structural topology of $P2_1/c$ clinopyroxenes, where two different tetrahedral sites are also found (Redhammer & Roth, 2003*b*) which are, however, situated in

two different chains. The overall changes of the tetrahedral bond lengths in $NaTiSi_2O_6$ with temperature are generally small (Fig. 12). In the *C*2/*c* phase the mean Si—O bond length tends to increase slightly with decreasing temperature towards the phase transition (Fig. 12*a*). This increase is dominated by the increase of the bond length between Si^{4+} and the O1 ('apex' of the tetrahedron) atom (Fig. 12*b*), which bridges tetrahedral and octahedral chains perpendicular to the tetrahedral chain direction (corresponding to [010] in *C*2/*c*). The larger Si—O3 bond lengths also tend to increase slightly with decreasing temperature (Fig. 12*c*), whereas the smaller Si—O3 (Fig. 12*d*) and the Si—O2 bond lengths remain constant (Fig. 12*e*). The O2 atom bridges the tetrahedral chain laterally (in *C*2/*c* this corresponds to the [100] direction) with the octahedral chain. In the triclinic low-temperature phase, $Si(1)O_4$ and $Si(2)O_4$ tetrahedra are different in size, with $Si(1)O_4$ being the largest. The variation of the individual Si(1)—O and Si(2)—O bond lengths do not show clear variations with temperature and the variations observable are within one estimated standard deviation. The average over the four individual Si—O bonds (Fig. 12*a*) however shows that in the triclinic phase the average Si(1)—O bonds tend to increase and the average Si(2)—O bonds become shorter. The average of the bridging Si—O bond lengths ($Si—O_{br}$) adopts a value of 1.643 (1) Å at 298 K, which remains almost constant in the *C*2/*c* phase; the same holds true for the $P\bar{1}$ phase. A slight decrease of the mean non-bridging Si—O bond lengths ($Si—O_{nbr}$) with increasing temperature might be inferred from Fig. 13 for the *C*2/*c* phase. In the triclinic phase the average value of the non-bridging Si—O bonds tends to increase with increasing temperature. Probably our temperature range is too small to deduce more reliable variations of $Si—O_{br}$ and $Si—O_{nbr}$ bond lengths, as observed by Cameron *et al.* (1973). For $NaCrSi_2O_6$, they observed a slight decrease of the mean $Si—O_{br}$ distance, whereas the mean of the $Si—O_{nbr}$ bond length increases with increasing temperature. For $NaFeSi_2O_6$, both the mean $Si—O_{br}$ and the mean $Si—O_{nbr}$ values are positively correlated with temperature (Cameron *et al.*, 1973). These observations suggest that no uniform behaviour of $Si—O_{br}$ and $Si—O_{nbr}$ as a function of temperature is to be expected.

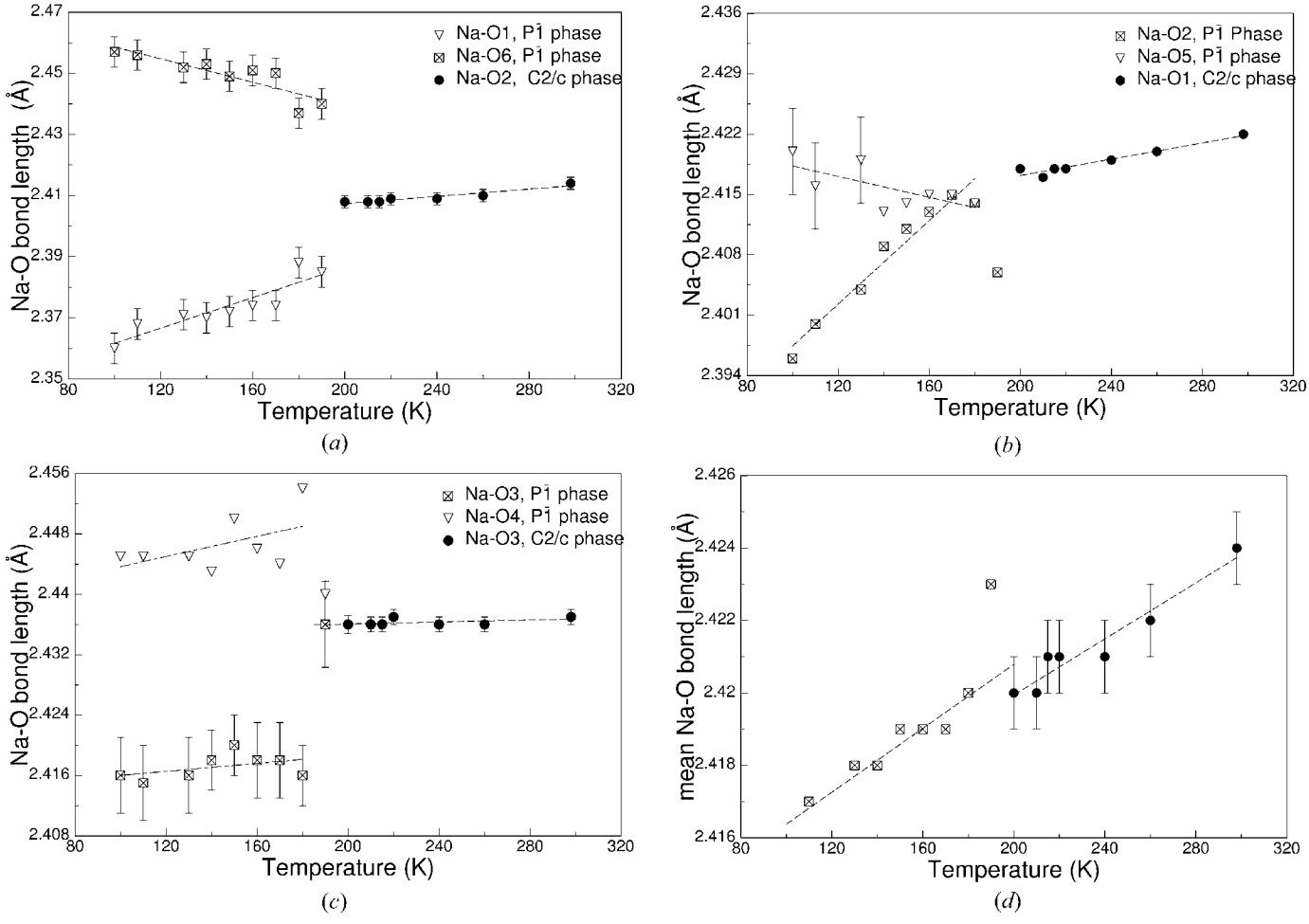

Figure 11
Individual and average Na—O bond lengths in $NaTiSi_2O_6$ *versus* temperature. Regression lines fitted to the data are guides to the eye and serve to clarify trends. Error bars are not shown for all the data points to keep figures clear. Error bars not shown are of similar size to those depicted.

As pointed out above (Fig. 4*a*), the mean of the four Si—O distances is dependent on the size of the cation occupying the *M*1 site in Na*M*Si$_2$O$_6$ clinopyroxenes. It is mainly the electronegativity, but also the electronic structure of the M^{3+} cation which influences the Si—O distances (Ohashi, 1981; Ohashi *et al.*, 1990). Ohashi (1981, 2003) and Ohashi *et al.* (1990) found that the difference $\Delta_{br\,-\,nbr}$ ($\Delta_{br\,-\,nbr}$ = average of the bridging Si—O distances minus average of the non-bridging Si—O distances) decreases with increasing the electronegativity of the M^{3+} cation in the Sc–Ti–V–Cr–Al series. The difference between the mean Si—O$_{br}$ and the mean Si—O$_{nbr}$ distances ($\Delta_{br\,-\,nbr}$) remains constant between 200 and 298 K, and is $\sim$0.031 Å in the monoclinic phase. However, in the triclinic phase $\Delta_{br\,-\,nbr}$ is distinctly larger in the Si1 site

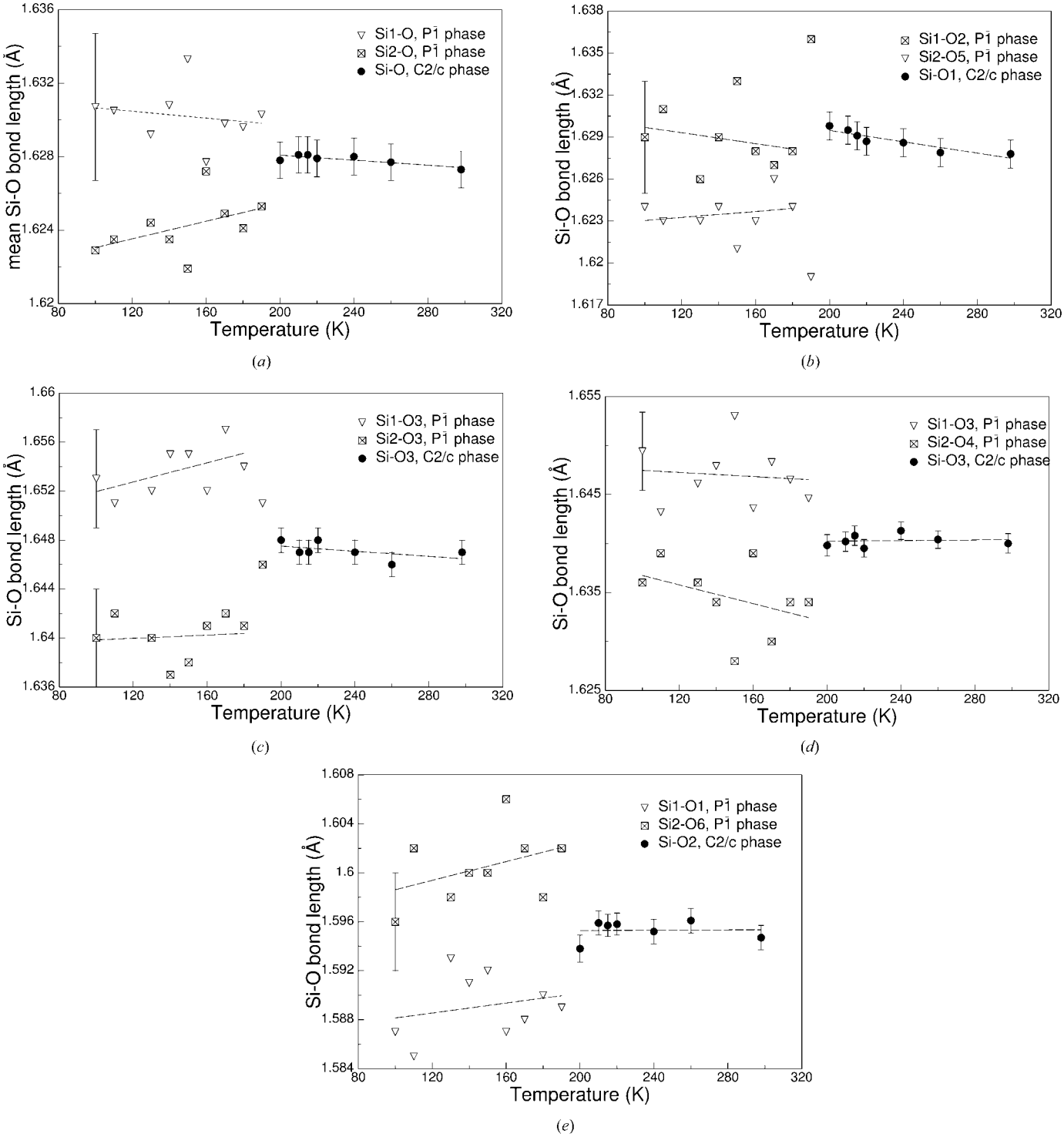

Figure 12
(*a*) Average and (*b*)–(*e*) individual Si—O bond lengths of NaTiSi$_2$O$_6$ *versus* temperature. Regression lines fitted to the data are guides to the eye and serve to clarify trends. Error bars are not shown for all datapoints to keep figures clear. Error bars not shown are of similar size to those depicted.

than in the Si2 site (Fig. 14*a*). Also, there are rather large changes within the O1—Si—O2 (*C*2/*c* phase), the O1—Si1—O2 and the O5—Si2—O5 ($P\bar{1}$ phase) bond angles at the phase transition point at 197 K (Fig. 14*b*). It is assumed that the localization of the one *d* electron of Ti^{3+} ($3d^1$ electronic configuration) results in a high screening constant in the direction of the O2 atom and in a charge up of the O2 atoms. High screening constants indicate electropositive character and charge up indicates an increase in repulsion effects. Therefore, Δ_{br-nbr} at the Si1 site is larger than at the Si2 site and the O1—Si1—O2 angle is larger than the O5—Si2—O6 angle. A localization of the *d* electron in the direction of the O2 atoms is consistent with the short Ti^{3+}—Ti^{3+} interatomic distance, observed across the O2—O2 octahedral edge.

In terms of bond-length distortion (BLD) and quadratic, tetrahedral angle variance (TAV), the $Si(1)O_4$ tetrahedron, which is the larger one, is more distorted than the $Si(2)O_4$ tetrahedron (Figs. 15*a* and *b*). The tetrahedral bridging angle (O3—O3—O3 in *C*2/*c*, O3—O4—O3 in $P\bar{1}$) decreases in *C*2/*c*, but increases in $P\bar{1}$ when temperature is lowered (Fig. 16*a*). The overall changes, however, are small compared with the very large changes observable for 1:3 clinopyroxenes, which transform from *C*2/*c* to $P2_1/c$. The Si—O—Si bond angle (Fig. 16*b*) decreases on temperature reduction over the complete temperature range with almost the same slope in *C*2/*c* and $P\bar{1}$. Therefore, the average Si—O—Si angle is positively correlated with the average Ti—O bond lengths, *i.e.* the decrease of the mean Ti—O with decreasing temperature results in a slight decrease in the elongation of the Si—O—Si bonds in the chain direction. The tetrahedral chains appear as a rather rigid unit which changes only slightly upon cooling. The small adjustments observable result from the different space requirements between octahedral and tetrahedral chains and are induced by the changes of the octahedral *M*1-site geometry.

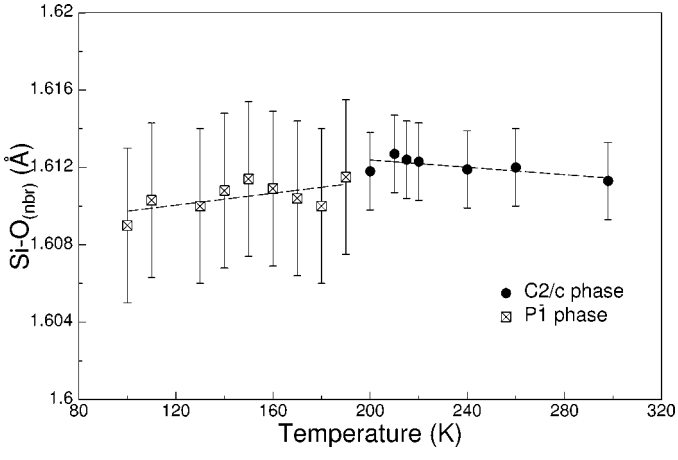

Figure 13
Variation of the average non-bridging Si—$O_{(nbr)}$ bond lengths within the SiO_4 tetrahedra as a function of temperature. Regression lines fitted to the data are guides to the eye and serve to clarify trends. For the *C*2/*c* phase, the displayed data are the mean out of two; for the $P\bar{1}$ phase the mean out of 4.

4. Conclusions

(i) The spin $\frac{1}{2}$ compound $NaTiSi_2O_6$ shows the space group *C*2/*c* at 298 K and is isotypic with other sodium clinopyroxenes. The structural parameters fit well into the trends deducible for the complete $NaMSi_2O_6$ series (*M* = Al, Ga, Cr, V, Fe, Ti, Mn, Sc and In).

(ii) The compound shows a crystallographic phase transition at 197 K, where the symmetry changes from *C*2/*c* directly to $P\bar{1}$. The general topology of the structure is similar in both the high- and the low-temperature phase. A main characteristic of the $P\bar{1}$ structure is the presence of two different Ti^{3+}—Ti^{3+} interatomic distances within the *M*1 octahedral chain. In contrast with the proposal of Ninomiya *et al.* (2003), there is only one crystallographically independent site for the Ti^{3+} atom. Yet the existence of two different Ti^{3+}—Ti^{3+} distances within the octahedral chain can still be interpreted as the formation of a dimer, which would be consistent with the spin-

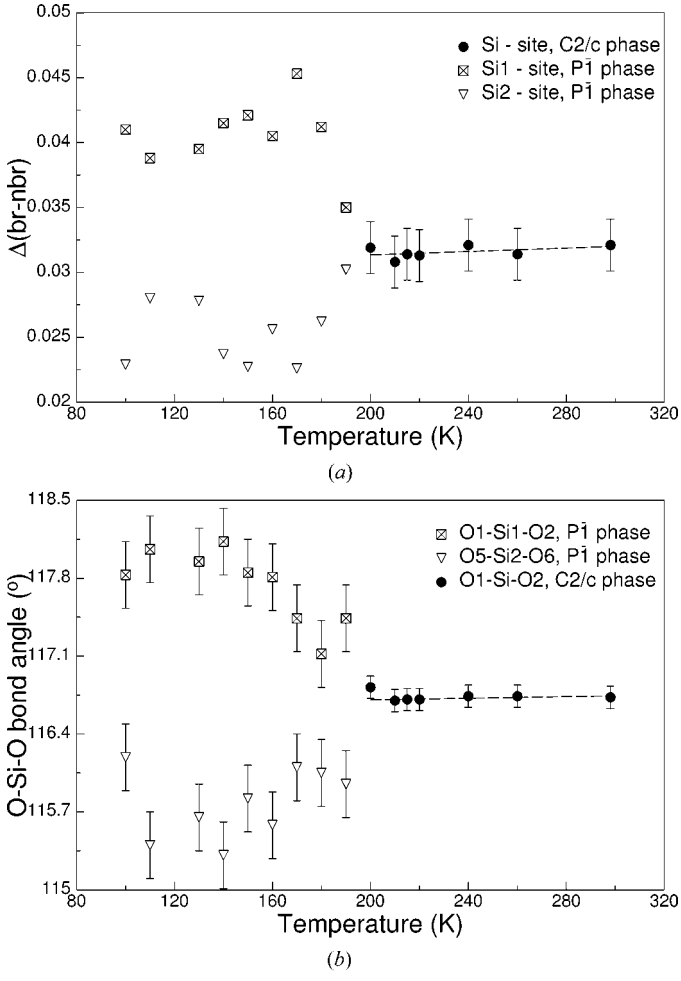

Figure 14
Variation of (*a*) the difference between the mean of the bridging Si—O bond lengths (Si—O_{br}) and the mean of the non-bridging Si—O bonds (Si—O_{nbr}), and of (*b*) the O—Si—O bond angle involving the O atom interconnecting the tetrahedral with the octahedral chain in [010] (*C*2/*c* phase) and [011] ($P\bar{1}$ phase) with temperature. Regression lines fitted to the data are guides to the eye and serve to clarify trends.

singlet ground state at low temperatures (Isobe *et al.*, 2002). This indicates a sudden development of singlet pairs below 200 K. Contrary to the results of Ninomiya *et al.* (2003), we found no gradual increase in the difference between the two $Ti^{3+}-Ti^{3+}$ pairs, but a discontinuous splitting by ~ 0.011 Å at the phase transition. Lowering the temperature further increases the difference between the two $Ti^{3+}-Ti^{3+}$ distances.

(iii) The correlations between the $M1-M1$ distances and the $M1-O-M1$ bond angles *versus* the mean $M1-O1$ bond lengths ($M1-O2$ and $M1-O5$ in the $P\bar{1}$ phase), as well as the variations in the $O1-Si-O2$ bond angles ($O1-Si1-O2$ and $O5-Si2-O6$ in $P\bar{1}$) and $\Delta_{br\ -\ nbr}$ with temperature suggest that the one t_{2g} electron of Ti^{3+} is localized towards the O2 atom within the octahedron.

(iv) The most rigid unit in the $NaTiSi_2O_6$ structure(s) upon cooling is the SiO_4 tetrahedron. The overall shrinkage in bond lengths is very small. The softest unit is the *M*2 site. Here mean $Na-O$ bond lengths shorten significantly with decreasing temperature. The mean $Ti-O$ bond lengths show inter-

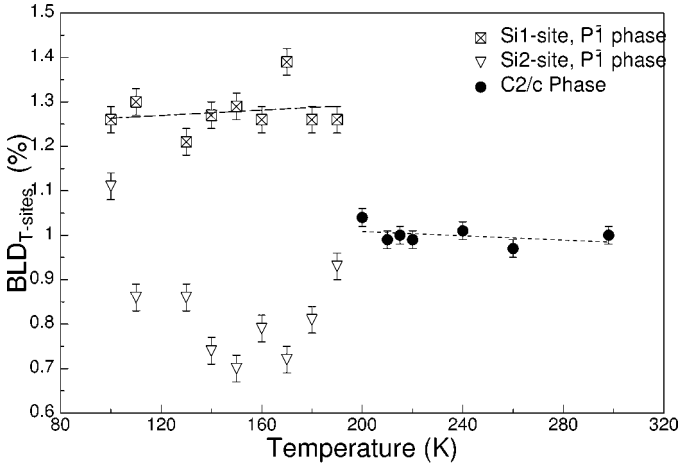

(*a*)

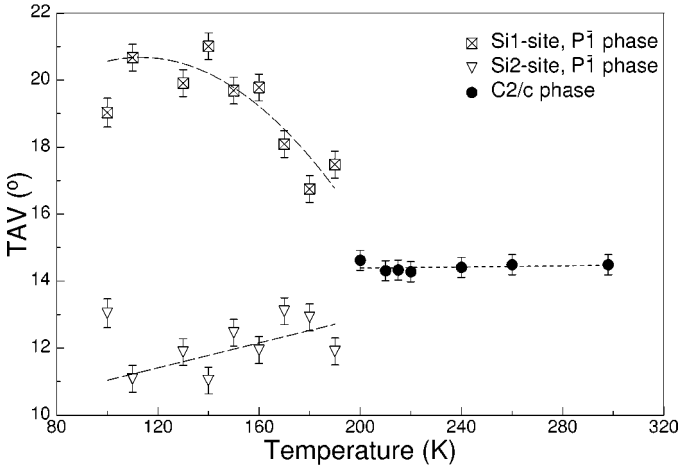

(*b*)

Figure 15
Polyhedral distortion parameters for the SiO_4 tetrahedron as a function of temperature: (*a*) bond-length distortion (Renner & Lehmann, 1986); (*b*) quadratic, tetrahedral angle variance (Toraya, 1981). Regression lines fitted to the data are guides to the eye and serve to clarify trends.

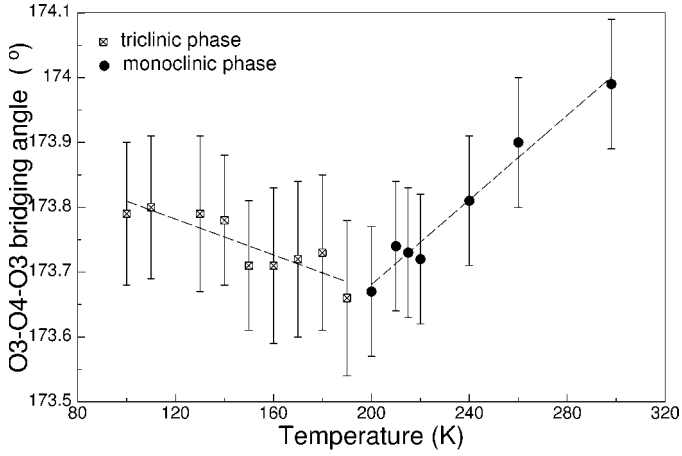

(*a*)

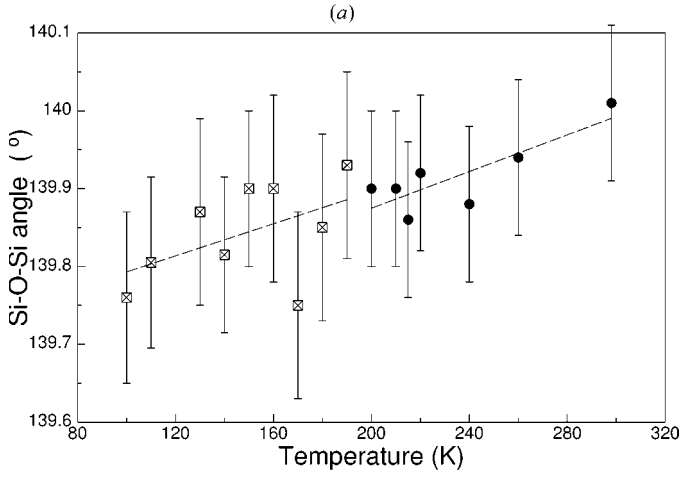

(*b*)

Figure 16
Interatomic angles, associated with the tetrahedral site, depicted as a function of temperature: (*a*) tetrahedral bridging angle; (*b*) $Si-O-Si$ bond angle (mean out of two for the $P\bar{1}$ phase). Regression lines fitted to the data are guides to the eye and serve to clarify trends.

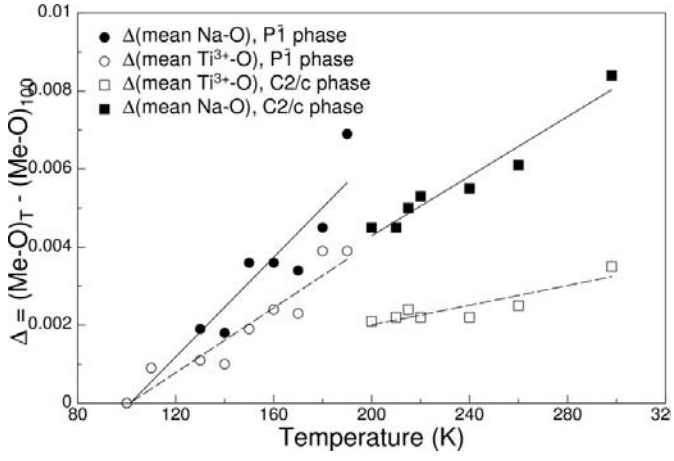

Figure 17
Comparison of the relative changes of averaged $Ti^{3+}-O$ and $Na-O$ bond lengths between 100 and 298 K, normalized to the values at 100 K. Regression lines fitted to the data are guides to the eye and serve to clarify trends.

mediate behaviour (Fig. 17). This is in excellent agreement with what has been found for other clinopyroxenes, when investigated as a function of temperature.

(v) In distinct contrast with the $C2/c \rightarrow P2_1/c$ phase transition, found especially in $LiMSi_2O_6$ clinopyroxenes (Redhammer & Roth, 2003*a*), no very large variations are found for the tetrahedral bridging angle. In the above-mentioned system, the tetrahedral bridging angle changes dramatically in the close vicinity of the phase transition (up to 10° within a few degrees Kelvin). Changing the tetrahedral kinking angle in $LiMSi_2O_6$ pyroxenes seems to be one of the possible ways to fit tetrahedral and octahedral chains in these structures. As can be seen in Fig. 16(*a*), changes in the tetrahedral bridging angle amount to less than 1° between 298 and 100 K in $NaTiSi_2O_6$. The different thermal expansion between the Mn, the *M*2 and the tetrahedral site is relaxed by several alterations in bond lengths and bond angles, but not by a specific kinking scheme. It is therefore concluded that the main factor, inducing the $C2/c \rightarrow P\bar{1}$ phase transition in $NaTiSi_2O_6$ and controlling the structural alterations, is the *M*1 octahedral site in general and the specific electronic nature of the trivalent titanium, leading to the formation of Ti^{3+}–Ti^{3+} pairs.

GJR acknowledges the financial support of the Austrian Academy of Science *via* an APART (Austrian Program for Advanced Research and Technology) scholarship (2000–2003).

References

Cameron, M., Sueno, S., Prewitt, C. T. & Papike, J. J. (1973). *Am. Mineral.* **58**, 594–618.
Clark, J. R., Appleman, D. E. & Papike, J. J. (1969). *Mineral. Soc. Am. Spec. Papers*, **2**, 31–50.
Downs, R. T. (2003). *Am. Mineral.* **88**, 556–566.
Farrugia, L. J. (1999). *J. Appl. Cryst.* **32**, 837–838.
Fukunaga, O., Yamaoka, S., Endo, T., Akaishi, M. & Kanda, H. (1979). *High-Pressure Sci. Technol.* **1**, 846–852.
Hawthorne, F. C. & Grundy, H. D. (1974). *Acta Cryst.* B**30**, 1882–1884.
Hawthorne, F. C. & Grundy, H. D. (1977). *Can. Mineral.* **15**, 50–58.
Isobe, M., Nimomiya, E., Vasil'ev, A. N. & Ueda, Y. (2002). *J. Phys. Soc. Jpn*, **71**, 1423–1426.
Konstantinović, M. J., van den Brink, J., Popovic, Z. V., Moshchalkov, V. V., Isobe, M. & Ueda, Y. (2003). Submitted; cond-Mater/0210191.
Ninomiya, E., Isobe, M., Ueda, Y., Nishi, M., Ohoyama, K., Sawa, H. & Ohama, T. (2003). *LT23 Proceedings*, submitted.
Ohashi, H. (1981). *J. Jpn. Assoc. Min. Petr. Econ. Geol.* **76**, 308–311.
Ohashi, H. (2003). *X-ray Study on Si—O Bonding.* Tokyo: Maruzen Publishing Service Center; ISBN 4–89630-094–7.
Ohashi, H., Fujita, T. & Osawa. T. (1982). *J. Jpn. Assoc. Min. Petr. Econ. Geol.* **77**, 305–309.
Ohashi, H., Fujita, T. & Osawa, T. (1983). *J. Jpn. Assoc. Min. Petr. Econ. Geol.* **78**, 159–163.
Ohashi, H., Osawa, T. & Sato, A. (1990). *Acta Cryst.* B**46**, 742–747.
Ohashi, H., Osawa, T. & Sato, A. (1994*a*). *Acta Cryst.* C**50**, 1652–1655.
Ohashi, H., Osawa, T. & Sato, A. (1994*b*). *Acta Cryst.* C**50**, 838–840.
Ohashi, H., Osawa, T. & Sato, A. (1995). *Acta Cryst.* C**51**, 2476–2477.
Ohashi, H., Osawa, T. & Tsukimura, K. (1987). *Acta Cryst.* C**43**, 605–607.
Prewitt, C. T. & Burnham, C. W. (1966). *Am. Mineral.* **51**, 956–975.
Redhammer, G. J. & Roth, G. (2003*a*). Submitted.
Redhammer, G. J. & Roth, G. (2003*b*). Submitted.
Redhammer, G. J., Roth, G., Paulus, W., Andre, G., Lottermoser, W., Amthauer, G. & Koppelhuber-Bitschnau, B. (2001). *Phys. Chem. Miner.* **28**, 337–346.
Renner, B. & Lehmann, G. (1986). *Z. Kristallogr.* **175**, 43–59.
Sheldrick, G. M. (1997*a*). *SHELXS*97. University of Göttingen. Germany.
Sheldrick, G. M. (1997*b*). *SHELXL*97. University of Göttingen. Germany.
Stoe & Cie (1996). *X-SHAPE* and *X-RED*. Stoe & Cie GesmbH, Germany.
Stoe & Cie (2002). *X-AREA*. Stoe & Cie GesmbH, Germany.
Toraya, H. (1981). *Z. Kristallogr.* **157**, 173–190.
Wilson, A. J. C. (1992). Editor. *International Tables for Crystallography*, Vol. C. Dordrecht: Kluwer Academic Publishers.